JOURNAL OF GEOPHYSICAL RESEARCH, VOL. 106, NO. A6, PAGES 10,883–10,904, JUNE 1, 2001

Dominant role of the asymmetric ring current in producing the stormtime *Dst**

M. W. Liemohn,[1] J. U. Kozyra,[1] M. F. Thomsen,[2] J. L. Roeder,[3] G. Lu,[4]
J. E. Borovsky,[2] and T. E. Cayton[2]

Abstract. Three storms are examined to determine the contribution to the *Dst** index from the symmetric and asymmetric (partial) components of the ring current. The storms (September 24-25, 1998, October 18-19, 1998, and May 14-15, 1997) all have a similar solar wind trigger (an initial shock followed by a coronal mass ejection with southward interplanetary magnetic field) and placement in the solar cycle (rising phase). The near-Earth ion distribution function is simulated for each storm using a kinetic transport model. The use of a McIlwain magnetospheric electric field description improves the simulation results over the Volland-Stern field used previously. It is found that most of the main phase magnetic field depression is due to the asymmetric component of the ring current (≥80% at the *Dst** minimum for the three storms). Note that this is a minimum asymmetric ring current contribution, because the closed-trajectory ions may also be spatially asymmetric. Ions in the partial ring current make one pass through the inner magnetosphere on open drift paths that intersect the dayside magnetopause. Changes in the density of the inner plasma sheet are transmitted directly along these open drift paths. For a steady convection field, an increase in the source population produces a decrease (more intense perturbation) in *Dst**, while a decrease produces a *Dst** recovery. As the storm recovery proceeds, a decrease in the electric field results in a conversion of open to closed drift paths, forming a trapped, symmetric ring current that dominates *Dst**. The mostly H^+ composition of the ring current for all three storms rules out the possibility of differential charge exchange being the cause of the fast and slow decay timescales, confirming that outflow is the main loss of ring current-generated *Dst** during the early phase decay. The slow decay timescale in the late recovery, however, is dominated by charge exchange with the hydrogen geocorona. The symmetric-asymmetric ring current is also placed in the context of the solar wind and plasma sheet drivers.

1. Introduction

The *Dst* (disturbance storm time) index is the average axial component of the horizontal disturbance field *D*, or the constant term in the Fourier expansion of *D* in local time, at any given UT, measured at four midlatitude stations widely spaced in local time [*Sugiura and Kamei*, 1991]. When the effects of magnetopause currents, induced currents in the conducting Earth, and the quiet time ring current are removed, the *Dst** index is created, which is thought to represent the ring current contribution. Observations [e.g., *Roeder et al.*, 1996; *Greenspan and Hamilton*, 2000] and simulations [e.g., *Kozyra et al.*, 1998a, b, c; *Jordanova et al.*, 1998a, b; *Ebihara and Ejiri*, 1998] indicate that the ring current is the main source of the *Dst** index during magnetic storms. Since the development of a strong ring current is a defining feature of magnetic storms [c.f., *Gonzalez et al.*, 1994], the *Dst* index has been adopted as a proxy for magnetic storm severity and geoeffectiveness of solar wind structures. A linear relationship exists between ring current kinetic energy and the *Dst** index for a symmetric ring current [*Dessler and Parker*, 1959; *Sckopke*, 1966].

Very successful *Dst* prediction schemes have been in use since the 1970s, based on solar wind energy input functions and empirically derived loss lifetimes [cf. *Burton et al.*, 1975; *Akasofu*, 1981; *Vassiliadis et al.*, 1999; *O'Brien and McPherron*, 2000]. Solar wind energy input functions used in these prediction schemes are based solely on heliospheric electromagnetic quantities. Statistical correlations between *Dst**, solar wind quantities, and geophysical parameters implicated in ring current formation and decay are leading to a more comprehensive understanding of what solar wind drivers are geoeffective. These studies, however, have no direct means of identifying the physical mechanisms responsible for the magnetospheric response to the geoeffective solar wind drivers.

A surprising statistical result has been the correlation between the solar wind E_y and not only the energy input function (as has been known for a long time [e.g., *Akasofu*, 1981]) but also the decay timescales for the ring current [*O'Brien and McPherron*, 2000]. The correlation between the solar wind motional electric field and the energy input to the magnetosphere has been previously demonstrated. However, the decay timescales during the main phase (at least for great storms) were thought to be determined by charge exchange lifetimes or wave-particle interaction timescales. We have shown that drifts of ring current ions on open drift paths to the dayside magnetopause provide the dominant loss during storm main and early recovery phases [*Liemohn et al.*, 1999]. That is,

[1]Space Physics Research Laboratory, University of Michigan, Ann Arbor, Michigan.
[2]Los Alamos National Laboratory, Los Alamos, New Mexico.
[3]Aerospace Corporation, El Segundo, California.
[4]High-Altitude Observatory, Boulder, Colorado.

Paper number 2000JA000326.
0148-0227/01/2000JA000326$09.00

convective drifts driven by the cross-tail electric field are responsible for the early rapid timescale decay of the ring current. The strength of this cross-tail electric field is directly proportional to the magnitude of the solar wind motional electric field. Larger solar wind electric fields lead to higher convection velocities and thus an increased rate of ion loss at the dayside magnetopause. This provides a natural explanation for the statistical correlation between solar wind E_y and decay timescales in the ring current .

However, convection electric fields are not the only driving function. It is now clear that significant changes in the density and temperature of the ring current source population in the inner plasma sheet also occur during the main phase [*Borovsky et al.*, 1997, 1998a; *Birn et al.*, 1997]. "Superdense" plasma sheet episodes have been observed, and plasma sheet density pulses have been seen traveling through the inner magnetosphere [*Borovsky et al.*, 1997, 1998b; *Thomsen et al.*, 1998]. These plasma sheet density enhancements are well correlated with high upstream solar wind densities, with time lags of 4-5 hours. It is not clear what proportion of the elevated plasma sheet density is due to solar wind entry and what proportion is due to ionospheric outflow. Ionospheric outflows are correlated with variations in the solar wind dynamic pressure [*Moore et al.*, 1999] and support for their importance can be found in the stormtime ring current composition [*Hamilton et al.*, 1988; *Daglis et al.*, 1993; *Grande et al.*, 1996].

Discrepancies were found between *Dst* derived from ring current ion observations (using linear theory and assuming a symmetric ring current) and *Dst* from ground-based magnetometers for selected storm intervals [*Hamilton et al.*, 1988; *Roeder et al.*, 1996]. These discrepancies triggered interest in carefully assessing the contributions from other current systems and from nonlinear processes (such as the influence of the ring current self-field) during the main phase buildup and early recovery of the magnetic storm. More recent observational studies of large numbers of storms [e.g., *Greenspan and Hamilton*, 2000] place the ring current contribution at 30-70% of the *Dst* index though there are errors in this estimate due to the local nature of satellite observations and the global nature of the *Dst* index. *Campbell* [1996] and *Alexeev et al.* [1996] challenged the paradigm that *Dst** is a measure of the symmetric ring current. *Campbell* [1996] attributed the *Dst* index during the main phase of magnetic storms to many superposed current contributions, one of them being the ring current. *Alexeev et al.* [1996] suggested that the main contributor to *Dst* is actually intensified magnetotail current, the disruption of which is responsible for the rapid early recovery of the *Dst* index during magnetic storms. The commonly used Dessler-Parker-Sckopke [*Dessler and Parker*, 1959; *Sckopke,* 1966] formula (DPS relation hereinafter) is based on the assumption of a nondivergent, symmetric ring current. This assumption is because only the cross-magnetic field currents in the magnetosphere ($\mathbf{J}_\perp$) are considered by this relation, while any field-aligned or ionospheric closure currents from $\nabla\bullet\mathbf{J}_\perp$ were omitted from its derivation. Yet large local-time asymmetry in the ring current during the storm main phase has been documented both in observations [*Roelof et al.*, 1987; *Hamilton et al.*, 1988; *Grafe*, 1999; *Greenspan and Hamilton*, 2000] and in models [cf. *Takahashi et al.*, 1990; *Liemohn et al.*, 1999; *Jordanova et al.*, 1999]. In fact, *Grafe* [1999, p. 1] states "only one ring current exists and this is an asymmetric one." As mentioned previously, model results indicate the partial ring current dominates in the storm main phase, early *Dst* recovery is controlled by drifts of ions to the dayside magnetopause, and the development of a symmetric ring current is a late recovery phase phenomenon [*Ebihara and Ejiri*, 1998; *Liemohn et al.*, 1999]. The presence of a large asymmetric component implies that field-aligned and ionospheric closure currents may make an important contribution to the *Dst* index.

The ring current is not the only contributor to the magnetic field perturbations used in deriving the *Dst* index. The field-aligned and ionospheric closure currents not represented in the DPS relation produce an approximately 20% positive offset in the estimated *Dst* index for the case of closure through an eastward electrojet [*Siscoe and Crooker*, 1974]. The weakening of the background magnetic field by the ring current self-field results in 7%-34% larger currents [cf. *Carovillano and Siscoe*, 1973]. The effects of the substorm current wedge can leak into the *Dst* index, producing positive contributions of up to a few tens of nanoteslas [*Friedrich et al.*, 1999]. A 25%-30% negative contribution to *Dst* is possible from enhanced magnetotail currents during magnetic storms and substorms [*McPherron*, 1997; *Turner et al.*, 2000]. A recent review of these contributing current systems is presented by *Greenspan and Hamilton* [2000].

The available satellite measurements, however, cannot determine how much of the ring current is on open or closed drift paths, and therefore how much of the *Dst* index is from the ion populations in each of these categories. In this study, three geomagnetic storms are analyzed to determine the breakdown of *Dst** contributions from the symmetric and asymmetric ring currents. In the next section, observations of the three storms are described, highlighting the geoeffectiveness of the various driver functions on the ring current. This is followed by a description of the numerical transport model used to simulate the ion phase-space distribution function in the inner magnetosphere. The data and results are then compared, followed by a discussion of what component (ions on open or closed drift paths) is responsible for the stormtime magnetic field perturbation. To briefly summarize, it is found that the stormtime ring current is mostly on open drift paths while the late recovery phase ring current is mostly on closed drift paths.

2. Observations of the Storms

It is clear that enhanced magnetospheric convection produced by intervals of southward interplanetary magnetic field (IMF) (negative IMF B_z) is an important element in building an intense ring current and producing a significant magnetic storm disturbance. The close relationship between strong negative IMF B_z ($\leq$ -10 nT) that lasts for 3 hours or more and large magnetic storms as indicated by *Dst* is a consequence of the central role of convection [cf. *Tsurutani and Gonzalez*, 1997]. It is becoming clear that, even near solar minimum, coronal mass ejections (CMEs) are responsible for major geomagnetic activity [*Gosling*, 1993; *Crooker and McAllister*, 1997; *Watari and Watanabe*, 1998]. CMEs are ejected from the base of the sector boundary between the coronal holes. The fastest ones are the most geoeffective because they sweep up the slower solar wind in front of them, compressing the plasma and fields to form a sheath region preceded by a shock [cf. *Tsurutani and Gonzalez*, 1997; *Kamide, et al.*, 1998; *McComas et al.*, 2000]. These shock-then-CME structures are thought to be very geoeffective (that is, producing major disturbances in the ionosphere and magnetosphere), particularly

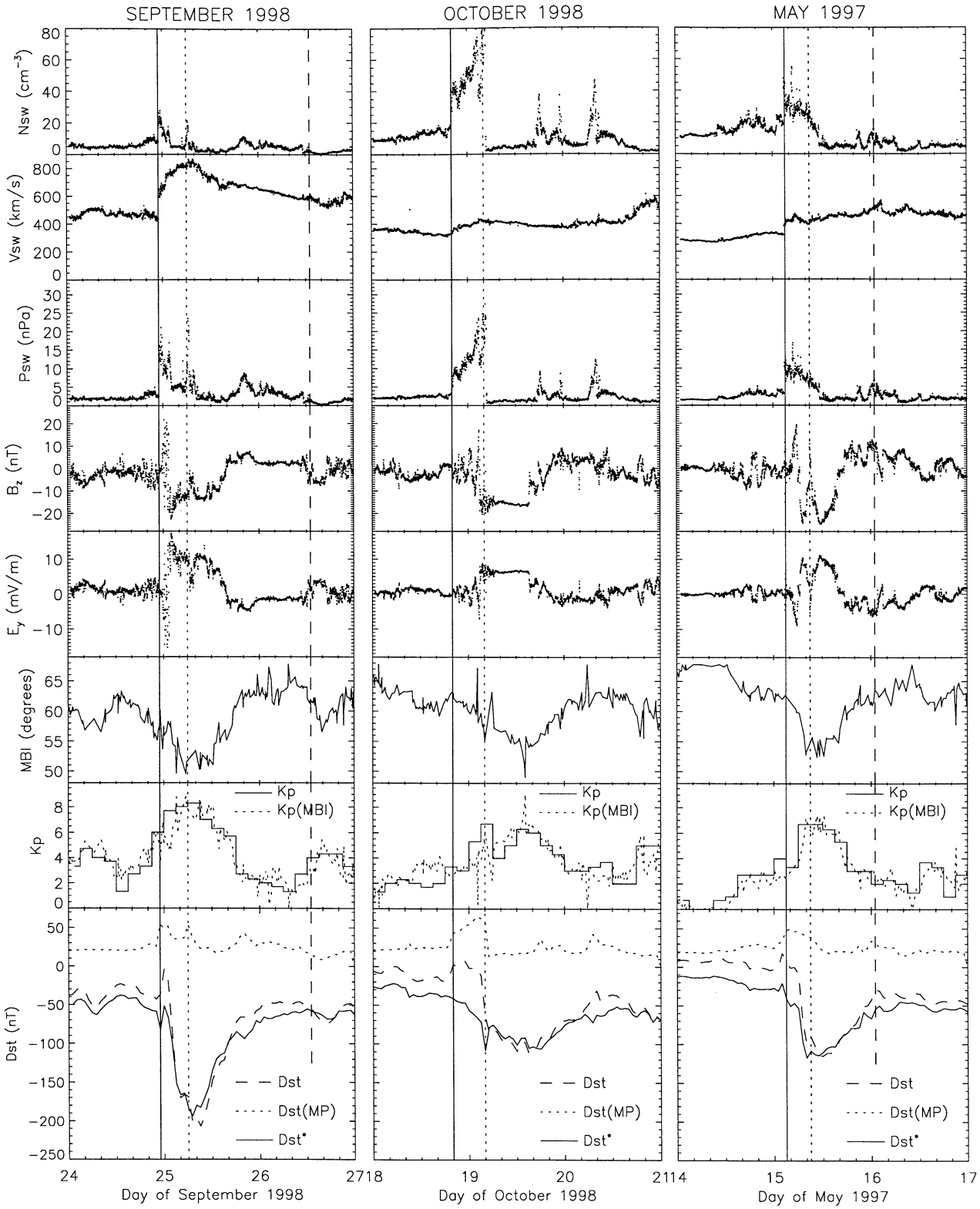

Figure 1. Solar wind and geophysical data during the three storms to be examined in this study: (left) September 1998, (middle) October 1998, and (right) May 1997. The rows are as follows: solar wind density, solar wind speed, solar wind dynamic pressure, north-south component of the interplanetary magnetic field, solar wind motion electric field, AFRL-produced midnight auroral boundary index, *Kp*, and *Dst*. The vertical lines through each column mark the following times: shock arrival (solid), shock-CME transition (dotted), and CME trailing edge (dashed). Note that the solar wind data have been time-shifted from Wind to the Earth.

when the IMF is southward during the shocked solar wind (hereinafter referred to as the sheath) and initial CME, increasing not only the magnetospheric convection but also allowing more efficient entry of solar wind plasma into the plasma sheet.

Three such storms have been selected for this study. They are the events of September 24-25, 1998, October 18-19, 1998, and May 14-15, 1997. These are interesting events not only for their similarity in solar wind structure and proximity in the solar cycle, but also because they are receiving much community attention as part of various comparative storm campaigns.

Figure 1 shows an overview of the observed solar wind features and geophysical responses (each column presents the data for a storm). In all three columns, the vertical solid line indicates the arrival of the shock at the magnetopause, the vertical dotted line shows the leading edge of the CME, and the vertical dashed line indicates the trailing edge of the CME at Earth (note that the ending of the CME for October 1998 is unclear and thus unmarked). The top five panels show the solar wind density, bulk flow speed, dynamic pressure, IMF Bz, and motional E_y=-V_{sw}×B_z, as seen by the Wind Solar Wind Experiment [*Ogilvie et al.*, 1995] and Magnetic Fields Instrument [*Lepping et al.*, 1995], time shifted from the Wind spacecraft to the Earth. WIND was upstream of Earth by 184 R_E, 107 R_E, and 193 R_E for the storms in September 1998, October 1998, and May 1997, respectively. It can be seen that the density makes a substantial jump at the shock front for each storm, followed by a significant decrease when the CME arrives at the Earth. The solar wind speed also increases at the shock. This results in a large pressure pulse, while the CME has much less dynamic pressure associated with it.

The fifth row of Figure 1 shows E_y, which is proportional to the solar wind energy input [*Burton et al.*, 1975]. During the September 1998 and May 1997 storms, strong southward B_z was embedded within the sheath preceding the CME, creating a large E_y (>10 mV m^{-1}) and a large energy input. In contrast, only weak and highly fluctuating B_z was present in the sheath preceding the October 1998 CME; thus there was no significant E_y or ring current energy input. In all cases, B_z (fourth row of Figure 1) turned sharply southward with the arrival of the CME and stayed strongly negative for about half a day, eventually turning northward again and settling near zero after the CME passage. The strongest storm (September 1998) had the weakest IMF B_z associated with the driving CME. It is clear that the strong solar wind velocity during the September 1998 storm produced a large E_y (up to 17 mV m^{-1}) and was responsible for the greater geoeffectiveness of this event compared to the other two.

The sixth row of Figure 1 shows the Air Force Research Laboratory (AFRL) midnight auroral boundary index [*Gussenhoven et al.*, 1981, 1983]. This is a measure of the latitude of the equatorward edge of the auroral oval at midnight, produced from DMSP satellite data using specific criteria to select appropriate orbits and map the value to local midnight (MBI hereinafter). It can be seen that this boundary drops well below 60° latitude during the storm, dropping after the shock and then rising as the IMF B_z turns northward. This is expected, because IMF B_z controls the magnetospheric convection strength, and MBI is a direct measure of the convection as it pushes the plasma sheet in toward the Earth. It is interesting to note that MBI does not mirror the functional form of IMF B_z, but rather drops in latitude during southward IMF and increases during northward IMF (that is, it is not constant during periods of steady IMF but instead exhibits some response timescale). Also note that in a dipole magnetic field, geosynchronous orbit maps to 67° latitude, so this boundary is well within this geocentric distance most of the time and almost always during a geomagnetic storm.

The seventh row of Figure 1 shows the planetary *K* index (*Kp*). The solid line is the observed value as produced by the World Data Center-C2 in Kyoto, Japan, while the dotted line shows the transformation of MBI into *Kp* using the empirical formula, *Kp*=67.8-MBI/2.07, derived by *Gussenhoven et al.* [1981]. There is excellent agreement between the two *Kp* values, demonstrating the robustness of the Gussenhoven formula. This also means that *Kp* exhibits the same growth and decay with IMF B_z that MBI exhibits. There are differences between the storms in MBI and *Kp* that should be pointed out. First, September 1998 was much stronger, with nearly a day of *Kp*≥6 (including 6 hours of Kp≥8) and an extended period of ~8 hours with MBI in the low 50s. October 1998 had only a few values of *Kp*≥6 and only a single MBI value down near 50°. May 1997, however, had a 9-hour period of *Kp*≥6, but just barely into this range, and MBI rarely dropped below 55° latitude.

Geoeffective elements in the solar wind driver produce dramatic responses in the *Dst* index, shown in the final row of Figure 1, from the World Data Center-C2 in Kyoto, Japan (dashed line). Also shown are two derivative disturbance perturbations, the positive perturbation caused by the magnetopause Chapman-Ferraro currents (dotted line) [*Burton et al.*, 1975], and *Dst** (solid line), which is *Dst* with the magnetopause and the Earth's diamagnetic effects removed [*Dessler and Parker*, 1959]. This final quantity is presumed to be a measure of the near-Earth current systems, most notably the ring current, but it also contains influences from other currents such as the near-Earth tail currents, high-latitude ionospheric currents, and substorm current systems. As evidenced in the previous two rows of data, *Dst* and *Dst** show a number of similarities and differences for the three storms. The September 1998 event reaches a minimum of less than -200 nT, while the other two storms barely cross the -100 nT level.

The sheath is the most geoeffective element during the September 1998 and May 1997 storms (even more geoeffective than the CME itself). In both cases, the *Dst** immediately responded to the strong southward IMF B_z in the sheath, sharply declined and reached nearly its minimum value prior to the arrival of the CME at Earth. Just after the CME arrival, *Dst** continued to decrease slightly, and then slowly recovered through most of the CME passage. Note, however, that E_y remains high after *Dst** has started to recover. This is a period of fast convection, meaning the near-Earth plasma sheet is being injected into the inner magnetosphere, yet *Dst** is decreasing instead of increasing. Recoveries in *Dst** are associated with more losses of ring current energy than inputs, and thus this period of high convection yet recovering *Dst** can be explained by a decrease in the plasma sheet source, causing a net loss of ring current particles as the dayside outflow exceeds the nightside inflow.

Despite having the largest dynamic pressure of the three events (see the third row of Figure 1), the October 1998 solar wind driver was much less geoeffective than the other two events. Following the shock and before the CME arrival (i.e., in the sheath), the IMF B_z was weak and highly variable, and E_y remained low. Without a geoeffective sheath (that is, one ac-

companied by IMF B_z<0) to trigger a rapid decline, the onset of the storm was much more gradual in *Dst**, reaching a minimum 10 hours after the arrival of the CME. In addition, E_y within the CME itself was smaller than the other two events, never exceeding 10 mV m^{-1}. Thus, particles were not driven through the inner magnetosphere for the October 1998 storm at nearly the same rate as for the other two storms.

One final thing to note is the close association between the length of the early recovery phase and the time interval for the solar wind E_y to recover from its maximum amplitude to small values at the trailing edges of the CMEs. This is consistent with the picture that as E_y weakens, open drift paths are gradually converted to closed drift paths, and the partial ring current to a symmetric trapped ring current. During this process, loss timescales switch from rapid "flow-out" losses associated with the partial ring current to much slower "charge-exchange" losses associated with the trapped symmetric ring current. This dramatic change in the loss lifetimes is the cause of the two-phase decay. Both September 1998 and May 1997 show very clear two-phase decays in *Dst**, while the decay of the October 1998 event is partially obscured by isolated pressure enhancements and a second (though smaller) disturbance on October 20 (associated with a rise in solar wind speed and a weak southward turning of IMF). The term "partially" is used here because a closer look at *Dst** reveals the transition between flow-out and charge-exchange timescales at approximately 0000 UT on October 20. A pressure enhancement also partially obscures the fast-to-slow timescale transition during the May 1997 recovery phase. Again, an examination of *Dst** shows evidence for this transition around 2000 UT on May 15. In all three cases, the early recovery phase occupies the same time interval as the change of the motional electric field in the CME from its maximum positive value to small values at the trailing edge of the CME. The steepest rate of change in E_y occurs for the September 1998 CME, followed by the May 1997 and then the October 1998 events. The fast decay timescales in the early recovery phase are roughly 8.5 hours, 13.5 hours, and 16.5 hours, respectively, mirroring the ordering from fast to slow rates of E_y decrease. The durations of the early recovery phase, and the period of sharp E_y decline in the CME, are 8 hours, 5 hours, and 8 hours, respectively. Clearly, the rate of change in E_y at the trailing edge of the CME is another element to consider in evaluating the geoeffectiveness of solar wind drivers and one that has not been previously considered.

Another data set with implications for ring current geoeffectiveness is the Los Alamos National Laboratory (LANL) geosynchronously orbiting satellites with their plasma spectrometers. The two main instruments are the magnetospheric plasma analyzer (MPA) that measures ions and electrons up to 50 keV [*McComas et al.*, 1993], and the synchronous orbit particle analyzer (SOPA) that measures the ions and electrons above 50 keV [*Belian et al.*, 1992]. In terms of ring current impact, the MPA energy range is the more important of the two, not only because of the larger energy density in this range but also because the particles in this energy range are less affected by gradient-curvature drifts and thus penetrate deeper into the inner magnetosphere. Therefore MPA observations are presented in Figure 2 for the three storms (along with the vertical lines from Figure 1, for temporal reference). These are composite pictures of velocity-space moments (100 eV- 50

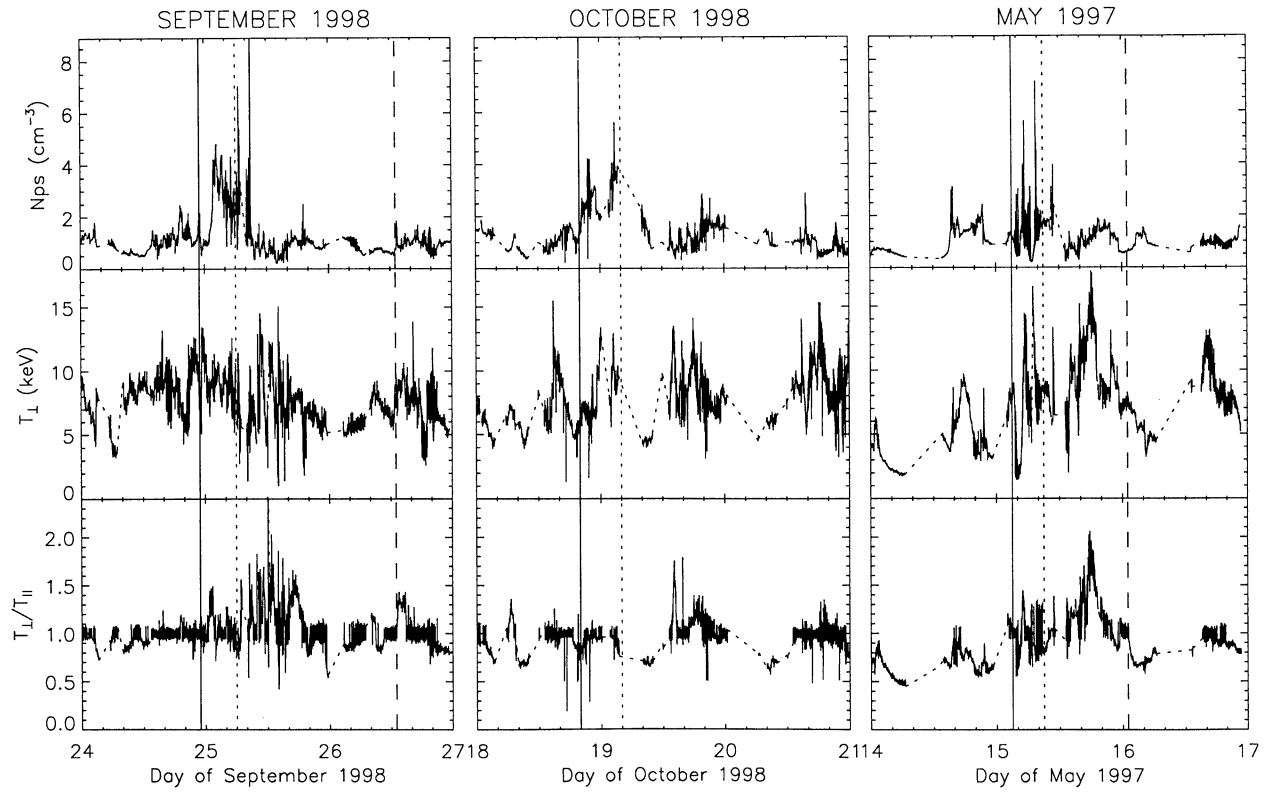

Figure 2. Moment calculations of the nightside plasma sheet observed by the MPA instruments on the LANL geosynchronous orbit satellites for the three storms (each column as in Figure 1). Shown are number density, perpendicular temperature, and the temperature ratio. Vertical lines are the same as in Figure 1, marking the times of the shock arrival and the leading and trailing edges of the CME.

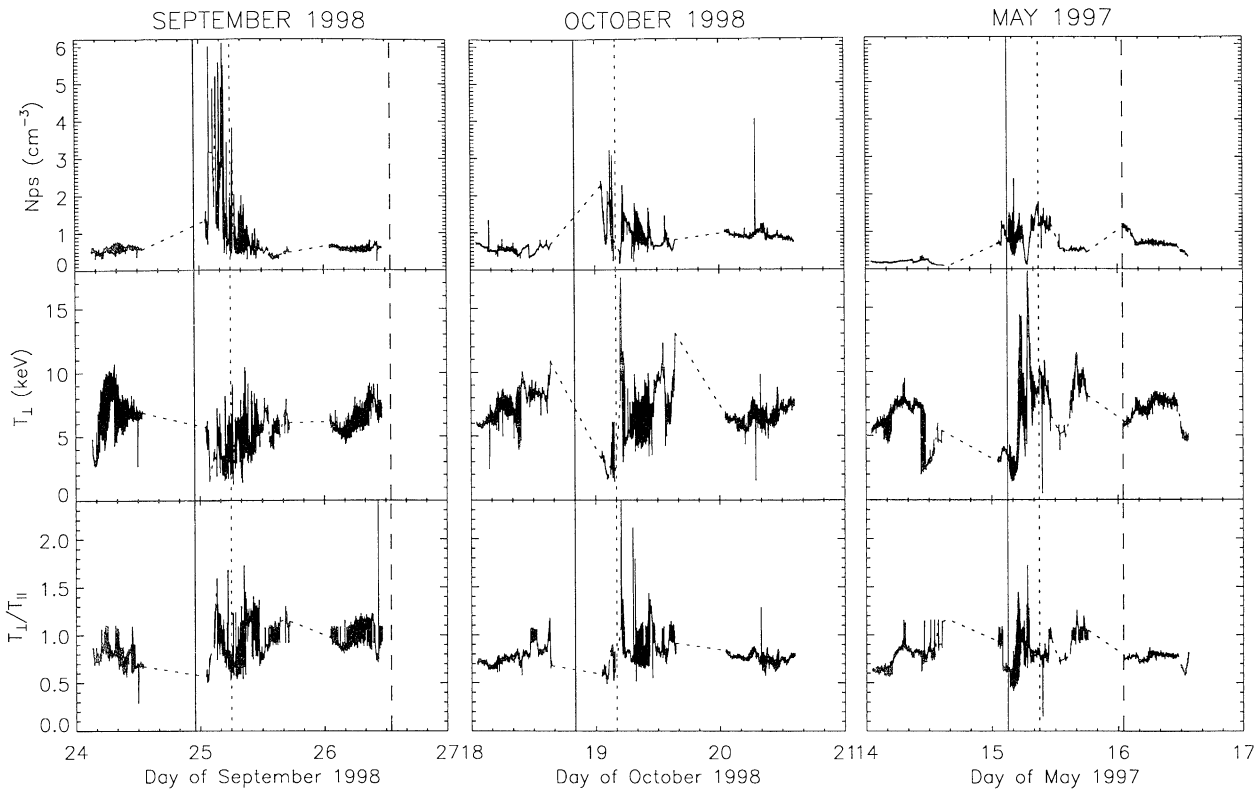

Figure 3. Moment calculations of the dayside plasma sheet observed by the MPA instruments on the LANL geosynchronous orbit satellites for the three storms (each column as in Figure 1). Shown are number density, perpendicular temperature, and the temperature ratio. Vertical lines are the same as in Figure 1, marking the times of the shock arrival and the leading and trailing edges of the CME.

keV) of ions that are drifting in from the near-Earth plasma sheet, with Figure 2 showing nightside plasma sheet values and Figure 3 showing dayside values. For the most part these are data from all of the satellites (up to five) whenever one is within 4 hours of local midnight, taking the measurement with the highest density when multiple satellites are in this range. The data set is expanded beyond (and, in certain instances, constricted from) this generic selection process according to other criteria as prescribed by the Los Alamos research team. That is, the energy spectrograms are scrutinized to maximize the plasma sheet observations usable as a nightside boundary condition while eliminating all non-plasma sheet observations from the data subset. Note that all three events have elevated plasma densities during the sheath, with a subsequent decrease in density during the CME. It is difficult to identify a trend in the temperature plots, with $T_\perp$ usually in the 5 to 10 keV range. In addition, the recovery phase of the storms all show enhanced anisotropies in this data set. Note that the moments are calculated assuming all of the measured particles are H^+, which underestimates the real ion density if there are significant numbers of heavier ions present. When used as an outer boundary condition for the ring current simulations, these densities are corrected according to a statistically predicted composition (discussed below).

Considering the timing of the shock arrival and CME leading and trailing edges with respect to the nightside near-Earth plasma sheet density, it is seen that the high-density interval ends soon after the arrival of the CME. Furthermore, comparing this timing with the solar wind E_y in Figure 1, it is seen that there is indeed an interval of high convection strength with low particle input density, yielding a period during the storms when the stormtime ring current is flushed out the dayside magnetopause and replaced with a weaker ring current. The rate at which this ring current swap occurs is directly related to the magnitude of E_y and the drop in plasma sheet density. Because the September 1998 storm had the largest of both of these quantities, it showed the fastest recovery of *Dst**. Conversely, the October 1998 storm had the smallest of both of these quantities, and it showed the slowest recovery of *Dst**. This (the timing of the decrease in E_y with respect to the decrease in N_{ps}) must also be taken into consideration, along with the recovery of solar wind E_y at the trailing edge of the CME, in determining the effectiveness of the driver functions in causing a rapid ring current decay.

These nightside plasma sheet values should be compared with the dayside values. Figure 3 shows a similar composite picture of velocity-space moments for the MPA observations within 4 hours of local noon. The most striking feature, of course, is the elevated densities during the sheath and early CME passage in all three storms. The $T_\perp$ profiles, which all show a minimum early in the sheath passage and then rise up to an average of 8-10 keV, provide a clue as to the source of these higher densities. The decrease in $T_\perp$ can be explained as the MPA measurement of the initial outflow of the low-energy portion of the preexisting ring current (the high-energy tail is dominated by the circular gradient-curvature drift motion around the Earth). The subsequent increase in $T_\perp$ raises this value up to very close to the nightside $T_\perp$ value, suggesting that these particles are fresh from the tail. In addition, the high-density interval always cuts off soon after the nightside

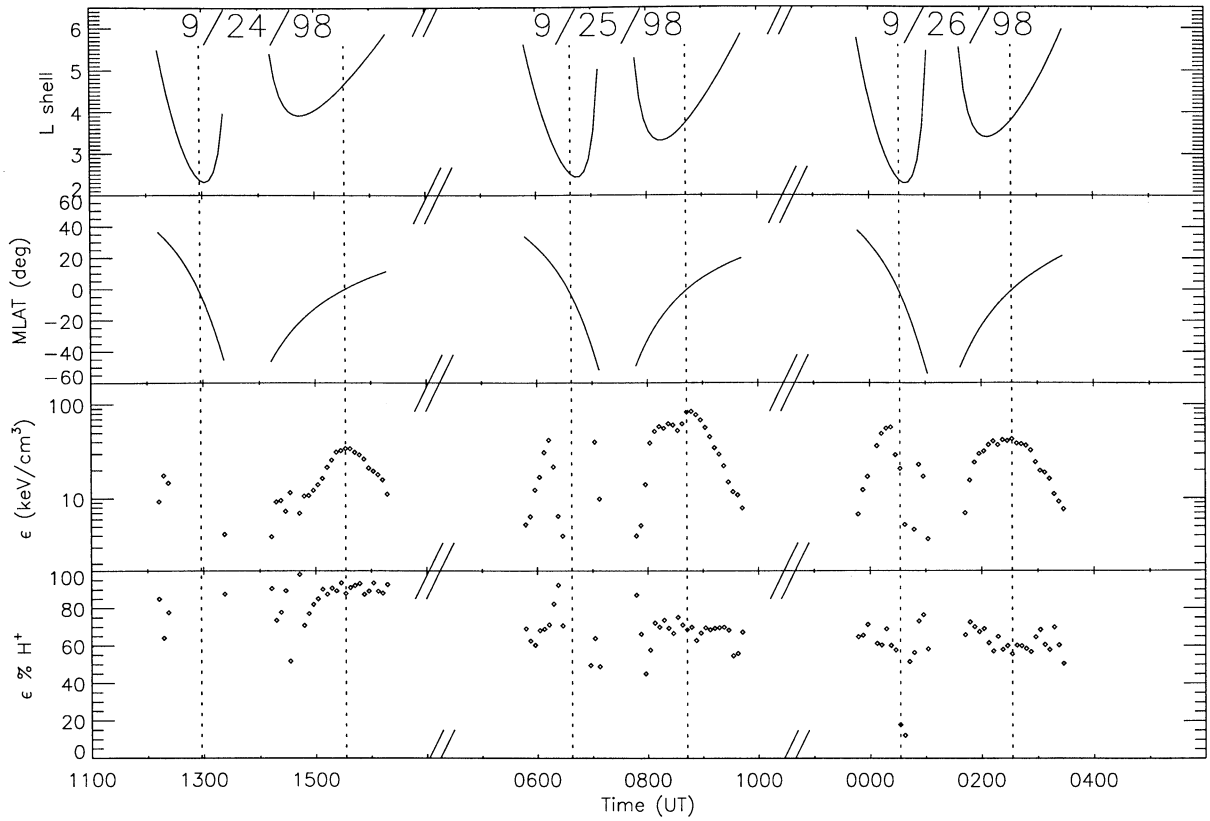

Figure 4. Polar-MICS observations of the ring current for three orbits during the September 1998 storm. The satellite L shell and magnetic latitude are shown in the top two panels, with the two passes for each orbit being the southbound dayside pass (~1300 LT) and the northbound nightside pass (~0100 LT). Also shown is the summed H^+ and O^+ local energy density (third panel) for $E \geq 30$ keV and the percent H^+ contribution to the energy density (fourth panel).

high-density interval seen in Figure 2. Furthermore, comparing Figure 3 with Figure 1 shows that the high densities on the dayside occur simultaneously with large positive E_y. This strong correlation with the nightside measurements and the convection strength imply that this is dayside outflow of a partial ring current (plasma sheet ions that passed close by the Earth on their single traversal through the inner magnetosphere).

In situ data from inside of geosynchronous orbit is available from the Magnetospheric Ion Composition Sensor (MICS) of the Charge and Mass Magnetospheric Ion Composition Experiment (CAMMICE) on the Polar spacecraft. MICS [*Chen et al.*, 1998] is very similar to the like-named instrument on the CRRES satellite [*Wilken et al.*, 1992]. Figure 4 shows the MICS data for three orbits during the September 1998 storm (for conciseness, only one storm will be shown). The top two panels show the location of the satellite for each orbit as a function of L shell and magnetic latitude, respectively. The first pass of each orbit pair sweeps from northern to southern latitudes on the dayside (~1300 LT) and the second pass of each pair from southern to northern latitudes on the nightside (~0100 LT). Note that the timescale has gaps to remove the long apogee passes of the orbit. The asymmetry of the spacecraft orbit is clearly seen. This is because apogee is not directly over the pole but instead shifted antisunward, and so the orbit passes closer to the Earth on the dayside than on the nightside. The first orbit is before the storm, the second is during the fast recovery, and the third is during the late recovery. Shown in the third panel of Figure 4 is the local energy density, integrated from the observed phase-space distributions. Note that only the high-energy data mode from the MICS instrument has been used (specifically, $E \geq 30$ keV for the integrals), because the low-energy mode is susceptible to contamination (probably from energetic electrons). The gaps in the presented data are because the integral was not used when there were ≤ 2 data points in the energy spectrum for either species (H^+ and O^+ were included in these integrals). The buildup and decay of the ring current can be clearly seen in these plots. In addition, the L shell of the peak of the ring current is usually evident several times each orbit. In the final panel of Figure 4 the percentage of H^+ contribution to the local energy density is shown. These plots demonstrate that H^+ is the major constituent of the near-Earth hot ion population. Although these storms occurred during the rising phase of the solar cycle, when the F10.7-cm solar luminance indicator is increasing (136, 120, and 75, for September 1998, October 1998, and May 1997, respectively), these values are not particularly high. This quantity has been correlated with the presence of ionospheric-origin plasma in the near-Earth plasma sheet [cf. *Young et al.*, 1982; *Lennartsson and Shelley*, 1986], and thus particles of ionospheric origin (O^+ and He^+, for instance) have small concentrations throughout the storms. This will be discussed in the Modeling Results section below.

3. Modeling the Ring Current

It is the intent of this study to examine quantitatively the contributions to *Dst* from ions on closed and open drift trajectories. Because the data coverage is sparse in the inner magnetosphere, this will be done with a kinetic transport model to simulate the near-Earth particle flow. The specific tool to be employed here is the Michigan version of the Ring Current-Atmosphere Interaction Model (RAM). The program solves the time-dependent, gyration- and bounce-averaged kinetic equation,

$$\frac{\partial f^*}{\partial t}+\frac{\partial}{\partial \vec{R}_\perp}\left\{\left\langle \frac{d\vec{R}_\perp}{dt}\right\rangle_{\vec{E}} f^*\right\}+\frac{\partial}{\partial E}\left\{\left\langle \frac{dE}{dt}\right\rangle_{\vec{E}} f^*\right\}+$$
$$\frac{\partial}{\partial \mu_0}\left\{\left\langle \frac{d\mu_0}{dt}\right\rangle_{\vec{E}} f^*\right\}=\frac{\partial}{\partial E}\left\{\left\langle \frac{dE}{dt}\right\rangle_{CC} f^*\right\}+\frac{\partial}{\partial \mu_0}\left\{\langle D_{CC}\rangle \frac{\partial f^*}{\partial \mu_0}\right\}$$
$$-\frac{f^*}{\tau_{CE}}-\frac{H(\mu_0-\mu_{0,LC})f^*}{0.5\tau_b} \qquad (1)$$

for the phase-space distribution function $f(t, R, \varphi, E, \mu_0)$ of a chosen ring current species [*Fok et al.*, 1993; *Jordanova et al.*, 1994, 1996, 1997; *Liemohn et al.*, 1998, 1999]. Note that f is related to f^* by a variable-dependent multiplier,

$$Q=\frac{Q^*}{R_0^2\mu_0 h(\mu_0)\sqrt{E}} \qquad (2)$$

needed for conversion to this conservative form of the kinetic equation [*Jordanova et al.*, 1994, 1996]. The five independent variables are, in order, time, geocentric distance in the equatorial plane (in units of R_E), magnetic local time (φ=0 at midnight, increasing eastward), kinetic energy (in keV), and cosine of the equatorial pitch angle. The code includes collisionless drifts (left-hand side terms), which are discussed in more detail below, energy loss and pitch angle scattering due to Coulomb collisions with the thermal plasma (first two terms on the right-hand side), charge exchange loss with the hydrogen geocorona (third term on the right-hand side), and precipitative loss to the upper atmosphere (last term on the right-hand side). The Heaviside function in the final term limits its application to pitch angles in the loss cone ($\mu_{0,LC}\leq\mu_0\leq 1$).

The source term for the distribution function is the outer simulation boundary, where observed particle fluxes from geosynchronous satellites (such as the data in Figure 2) are applied as input functions. All of the simulations discussed below use geosynchronous plasma sheet measurements as the outer boundary condition. Because the MPA and SOPA instruments do not resolve ion mass, the composition of the incoming particles is determined from the statistical relationships derived by *Young et al.* [1982] from previous geosynchronous orbit measurements [*Liemohn et al.*, 1999]. Note that the plasma boundary condition, while having a high time resolution (~100 s cadence), is applied uniformly over the nightside outer boundary. This sacrifice in spatial variability is thought to be acceptable because of the relative uniformity of the near-Earth plasma sheet [cf. *Huang and Frank*, 1986; *Baumjohann et al.*, 1989; *Borovsky et al.*, 1998b; *Thomsen et al.*, 1998].

Solution of the kinetic equation is accomplished by replacing the derivatives with second-order accurate, finite volume, numerical operators. The chosen technique uses the method of fractional steps [*Yanenko*, 1971] to solve each term separately while maintaining second-order accuracy [*Fok*, 1993]. The numerical grid step sizes were chosen to resolve the features of interest, maintain numerical stability and accuracy, and optimize the run-time of the simulation. The grid used in each variable is as follows: 20 s time step; 20 equally spaced radial steps from 2 R_E to 6.5 R_E geocentric distance; 24 equally spaced points in local time around the Earth; 42 geometrically spaced energy cells from 10 eV to 350 keV; and 70 pitch angle grid points from 0° to 90° (0 to 1 in μ_0). This results in a few thousand velocity space cells at each of a few hundred spatial locations, for a total of ~1.4 million phase space cells. Each of these cells contains one unknown, f, and they are all coupled through (1). Because the kinetic equation is linear in this form (that is, none of the coefficients depend on f), each hot plasma species can be calculated individually with the results summed later to obtain such bulk quantities as *Dst** or current density. For these simulations the major ring current species of H^+ and O^+ will be computed. The gyration and bounce-averaged approach is quite appropriate for the ring current ions, whose Larmor period (~0.1-10 s) and bounce period (~10-1000 s) are much less than the typical loss lifetimes (hours to days). However, a kinetic approach is still necessary because the distribution is far from Maxwellian, particularly as the particles differentially drift through the inner magnetosphere.

Several other models are also used to describe the background conditions during the simulations. Linked codes that provide background values for the calculation are the *Rasmussen et al.* [1993] dynamic plasmasphere model, the *Rairden et al.* [1986] geocorona description, and the *Shue et al.* [1998] magnetopause location. The plasmasphere model also uses the International Reference Ionosphere model [*Bilitza*, 1986] and the Mass Spectrometer Incoherent Scatter thermospheric model [*Hedin*, 1987] for aeronomical inputs. In addition to these inputs, the transport model requires electric and magnetic field descriptions. The magnetospheric electric field uses the MBI-driven *Kp* value for its activity dependence (see Figure 1). The benefit of using the MBI-derived *Kp* value is that it contains far more structure on a much faster timescale (tens of minutes between index values rather than the 3-hour cadence of the regular *Kp* index), allowing for a more realistic convection pattern evolution during the storm.

4. Drift Velocity Terms

Several terms are included in the bounce-averaged drift velocities. The first is the corotation drift, created because the field lines are anchored at the Earth's surface. This has a potential of

$$\Phi_{co}=-\frac{C_{co}}{R}, \qquad (3)$$

where C_{co}=92 kV R_E is the corotation strength coefficient. This can be converted into a drift by differentiating (to get the electric field) and vector crossing with the magnetic field, which results in an azimuthal drift term (assuming a dipole magnetic field),

$$\left\langle \frac{d\varphi}{dt}\right\rangle_{co}=\frac{C_{co}}{M_E}, \qquad (4)$$

where M_E=8x10^{15} Tm^3 = 1.26x10^6 kVs R_E is the magnetic moment of the Earth. Given in radians/s, this drift is constant with radial distance and moves particles around the Earth in one day.

Another term is the magnetospheric convection drift, created by the cross-polar cap potential difference driving a dawn-

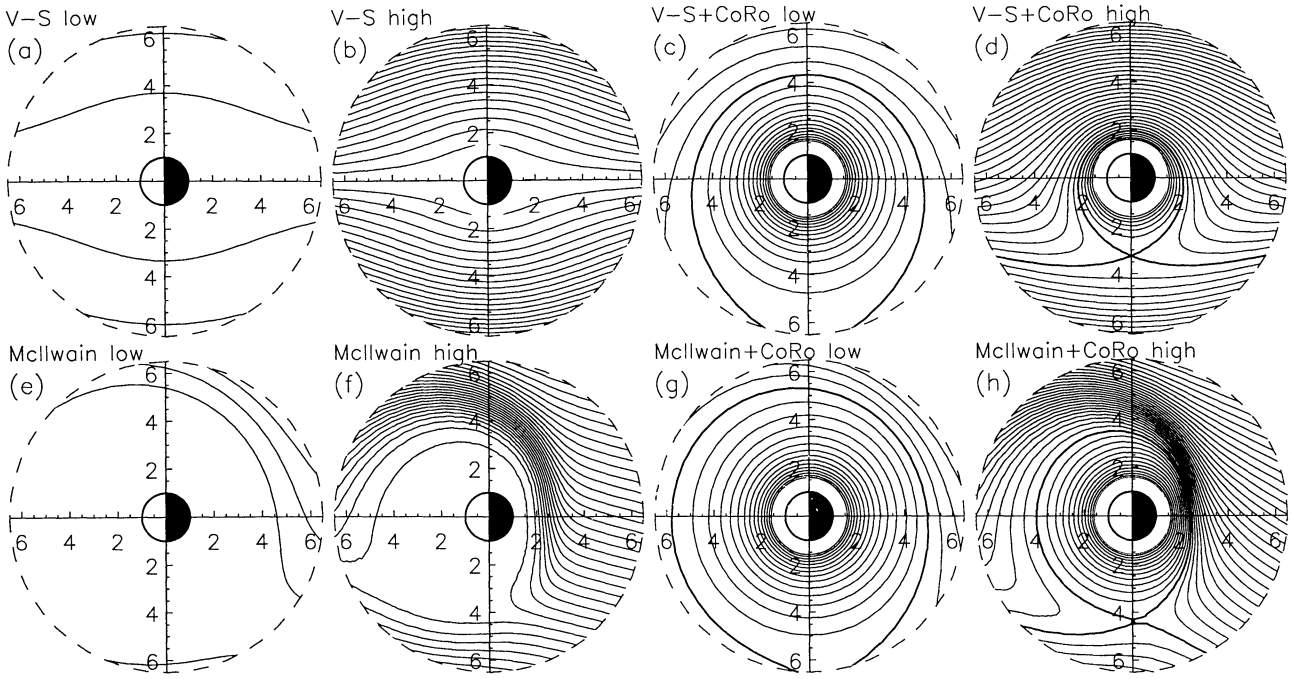

Figure 5. Equipotential contour maps for the two magnetospheric electric field descriptions: (a-d) Volland-Stern field and (e-h) McIlwain field. The first two columns are for low and high geomagnetic activity (see the text), respectively, and the next two columns are the same plots with the corotation potential added in to the map. Equipotential contours are spaced every 3 kV, and the dark solid line is the last closed equipotential. Note that these are also the zero-energy particle drift trajectory maps.

dusk electric field in the magnetotail. There are many descriptions of this field, but two analytical forms will be discussed here. The first is the Volland-Stern magnetospheric convection electric field [*Volland*, 1973; *Stern*, 1975], which has a potential of

$$\Phi_{VS}=AR^2\sin\varphi \tag{5}$$

where A is the activity-dependent strength coefficient taken from *Maynard and Chen* [1975],

$$A=\frac{0.0449}{\left(1.-0.159Kp+0.0093Kp^2\right)^3}\left[\frac{kV}{R_E^2}\right], \tag{6}$$

and a shielding factor of 2 has been assumed (standard shielding, see *Maynard and Chen* [1975] for details). This yields a purely dawn-dusk electric field at large R, but a weaker field near the Earth. Note that if $R\to\infty$ then $\Phi_{VS}\to\infty$, and therefore (5) should only be used in the inner magnetosphere. The radial and azimuthal drifts from (5) are

$$\left\langle\frac{dR}{dt}\right\rangle_{VS}=-\frac{AR^4\cos\varphi}{M_E} \tag{7a}$$

$$\left\langle\frac{d\varphi}{dt}\right\rangle_{VS}=\frac{2AR^3\sin\varphi}{M_E}\,. \tag{7b}$$

The drift trajectories of particles in this field are not purely sunward but rather bend away from the Earth in an elliptical deflection near the planet. Figures 5a and 5b show equipotential contours from (5) (streamlines from (7)) for low and high magnetic activity (Kp=2 and 8, respectively), while Figures 5c and 5d are the same plots with the corotation potential (3) added in. The density of the lines gives a rough estimate of the flow strength (contours every 3 kV). In these dial plots the view is from over the North Pole, with the Sun (local noon) off to the left. Flow is in from the right-hand (nightside) boundary and out the left-hand (dayside) boundary, with the corotation flows near the Earth in the counterclockwise (eastward) direction. These contours are also the flow paths of the zero-energy particles. Figures 5c and 5d show the classic teardrop shape of the separatrix between open and closed drift trajectories (equipotentials that do or do not reach the magnetopause, respectively). The size of the separatrix is a function of activity, and the shape is a function of the shielding parameter. Note that the outer limit of the dial plots is at geosynchronous orbit (R=6.6), which is the outer boundary of the simulation domain.

Another analytical representation of the global electric field is the McIlwain magnetospheric drift description [*McIlwain*, 1986], which was inferred from geosynchronous orbit data and has the form

$$\Phi_{Mc}=\kappa H\left[R\left(E_{Mc,y}\sin\varphi+E_{Mc,x}\cos\varphi\right)+\Phi_{off}\right], \tag{8}$$

where κ is an activity-dependent strength coefficient (see below), H is a shielding function

$$H=\frac{1}{1+\left(R_0/R\right)^8} \tag{9}$$

that depends not only on R but also on φ and Kp through the characteristic shielding distance R_0,

$$R_0=0.8\left[9.8-1.4\cos\varphi-\left(0.9+0.3\cos\varphi\right)K_r\right] \tag{10}$$

in units of R_E. In (10), K_r is a reduced Kp index, $K_r=Kp/(1+0.1Kp)$. In *McIlwain* [1986], $E_{Mc,x}$, $E_{Mc,y}$, and Φ_{off} were given the values 0.2 kV/R_E, 0.8 kV/R_E, and 3 kV, respectively. The potential given by (8)-(10) results in a rotated and offset electric field from the dawn-dusk direction (a predawn to predusk electric field), with a shielding-induced near-Earth reduction that is more pronounced on the dayside than on the nightside. As above, (8) can be converted into radial and azimuthal drifts,

$$\left\langle \frac{dR}{dt} \right\rangle_{Mc} = \frac{R^3 \kappa H}{M_E}\left[E_{Mc,y}\cos\varphi - E_{Mc,x}\sin\varphi - 8H\sin\varphi\left(E_0 + \frac{\Phi_{off}}{R}\right)\frac{R_0^7}{R^8}(1.12+0.24K_r)\right] \quad (11a)$$

$$\left\langle \frac{d\varphi}{dt} \right\rangle_{Mc} = -\frac{R^2 \kappa H E_0}{M_E}\left[1+8H\left(1+\frac{\Phi_{off}}{RE_0}\right)\left(\frac{R_0}{R}\right)^8\right], \quad (11b)$$

where the substitution $E_0=E_{Mc,y}\sin\varphi+E_{Mc,x}\cos\varphi$ has been used. The strength coefficient κ prescribed by McIlwain is $\kappa=1+0.3K_r$, which is less than linear with Kp. This is unrealistic, however, because Kp is a pseudo-logarithmic scale of the real activity level. This nonlinearity between Kp and activity is seen in (6) for the *Maynard and Chen* [1975] A coefficient for the Volland-Stern model. Therefore, rather than guessing at a proper functional form of κ with Kp, the McIlwain convection will be scaled to the real convection strength as governed by the cross-polar cap potential difference $\Delta\Phi_{pc}$, normalizing the total potential drop across the magnetosphere from (8) by this value,

$$\kappa = \frac{\Delta\Phi_{pc}}{\left[R_{MP}(\varphi=\pi/2) - R_{MP}(\varphi=3\pi/2)\right]\max\left[E_0\right]}, \quad (12)$$

where R_{MP} is the radial distance to the magnetopause (in the dawn and dusk directions), found from the *Shue et al.* [1998] magnetopause description from the upstream solar wind conditions. Figures 5e and 5f show the equipotential pattern from (7) for low and high activity strength, respectively (low: Kp=2, ΔR_{MP}=30 R_E, $\Delta\Phi_{pc}$=40 kV; high: Kp=8, ΔR_{MP}=20 R_E, $\Delta\Phi_{pc}$=150 kV), and Figures 5g and 5h show these patterns again with the corotation potential included. It is seen that the McIlwain field now has a similar amplitude range as the Volland-Stern electric field description, but with a more realistic flow pattern through the inner magnetosphere. The teardrop is deformed, pushed in on the nightside with a stagnation point (the tip of the teardrop) extended out in radius. This shape is more in line with observed drift boundaries [e.g., *Chappell et al.*, 1970, 1971; *Gussenhoven et al.*, 1981, 1983; *Carpenter and Anderson*, 1992; *Moldwin et al.*, 1994; *Elphic et al.*, 1996; *Weiss et al.*, 1997; *Ober et al.*, 1997]. Note that the main source of difference between the Volland-Stern field and the McIlwain field is the shift in orientation of the latter away from noon-midnight symmetry toward morning-evening. This is generated by the $\cos\varphi$ term in (8), and a similar offset in (5) would also cause this rotation.

In addition to the drift in R and φ, the particles will drift in energy and pitch angle by conservation of the first and second adiabatic invariants. These rates of change may be written as functions of the radial drift velocity [*Jordanova et al.*, 1996],

$$\left\langle \frac{dE}{dt} \right\rangle = -\frac{3E}{R}\left[1-\frac{I}{6h}\right]\left\langle \frac{dR}{dt} \right\rangle \quad (13a)$$

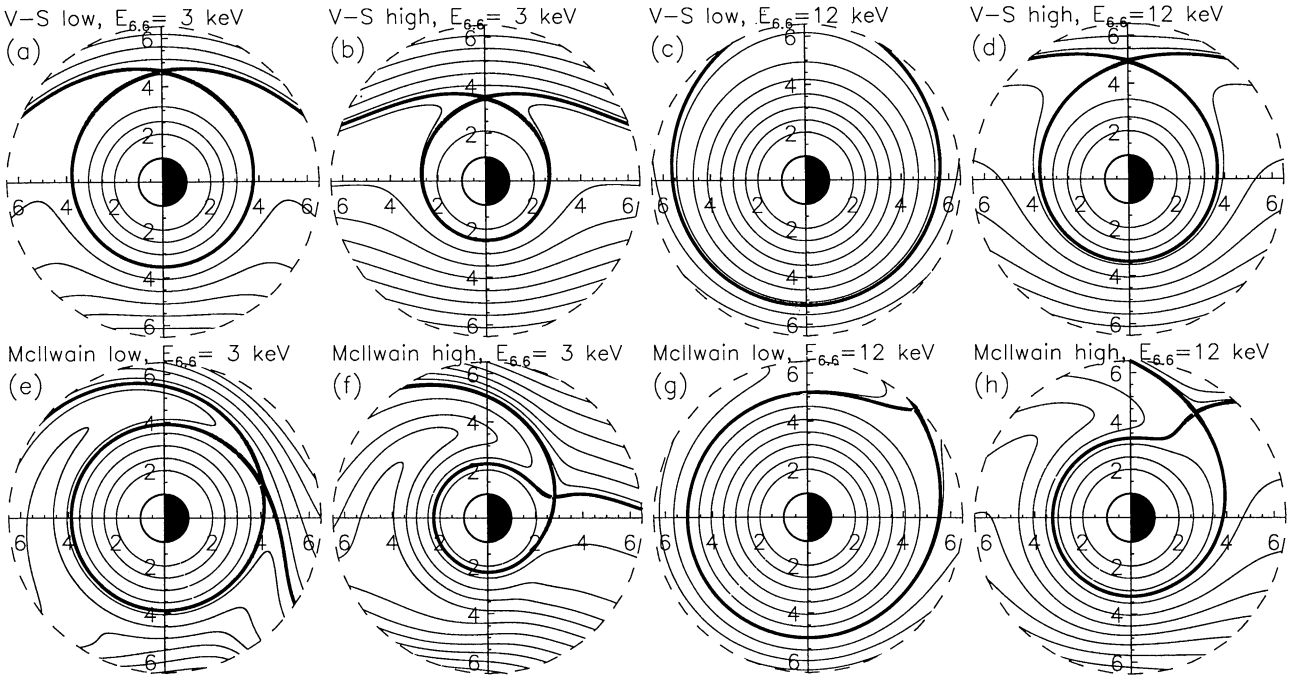

Figure 6. Drift trajectory maps for the two magnetospheric electric field descriptions: (a-d) Volland-Stern field and (e-h) McIlwain field, including corotation and gradient-curvature effects. The first two columns are for $E_{6.6}$=3 keV for low and high activity (see the text), respectively, and the next two columns (c, d, g, h) are for $E_{6.6}$=12 keV for low and high activity, respectively. The dark solid line is the last closed drift trajectory, and the placements of the other lines are arbitrarily chosen.

$$\left\langle \frac{d\mu_0}{dt} \right\rangle = \frac{\left(1-\mu_0^2\right)}{4R\mu_0} \frac{I}{h} \left\langle \frac{dR}{dt} \right\rangle . \quad (13b)$$

These drift terms simply increase the energy as the particle moves closer to the Earth (negative radial drift), and decrease μ_0 (increase the pitch angle) as the particle moves closer to the Earth. The I and h variables are bounce-averaging terms that reduce to analytical functions of μ_0 in a dipole magnetic field [*Ejiri*, 1978].

A final drift term that must be included in the bounce-averaged velocities is the azimuthal flow from the fact the magnetic field has both a gradient and a curvature. For a dipole magnetic field, this drift term has the form [*Bittencourt*, 1986]

$$\left\langle \frac{d\varphi}{dt} \right\rangle_{GC} = -\frac{3ER}{qM_E}\left[1-\frac{I}{6h}\right] \quad (14)$$

and can be expressed as the gradient of an effective potential,

$$\Phi_{GC} = -\frac{3E \ln R}{q}\left[1-\frac{I}{6h}\right] . \quad (15)$$

Because of the energy and pitch angle dependence of (15), a curve of constant Φ_{GC} is not a particle streamline through the magnetosphere because energy and pitch angle change according to (13) as the particle radially drifts. Thus a plot of this potential, like those shown in Figure 5, is not particularly meaningful.

The influence of the gradient-curvature drift can be seen in maps of the trajectories from all of the drift terms. Figure 6 shows such maps of ion trajectories for low and high activity (as presented in Figure 5), for a medium and high energy (low energy, singly charged particles of either charge sign and any mass follow the equipotential lines shown in Figure 5), for the Volland-Stern field (top row) and the McIlwain field (bottom row). By setting the derivatives of the potential with respect to R and φ equal to zero, and taking into account that E and μ_0 change with R, the stagnation point can be found, and the trajectory through this point has been drawn as the dark solid line. The rest of the contours are chosen to best show the flow pattern (unlike Figure 5, where they are evenly spaced equipotentials). The chosen energies are 3 and 12 keV at 6.6 R_E, which are typical low and high values of characteristic ion energies observed at geosynchronous orbit. These energies correspond to M=0.0278 and 0.111 keV nT^{-1}, respectively (M is the first adiabatic invariant value). These two chosen values, when discussing trajectories through the inner magnetosphere, will be referred to as $E_{6.6}$ energies. For reference a particle with E=3 keV at R=6.6 will have E=13.5 keV at R=4 and E=108 keV at R=2 in a dipole field. The pitch angle chosen for the plots in Figure 6 is 90° (equatorially mirroring), which removes the μ_0 dependence of the drifts (although this effect is not neglected in the model calculations). The teardrop is flipped because the gradient-curvature drift overpowers the corotation drift, especially at such high energies (flow is clockwise on the closed trajectories). However, while the Volland-Stern field always has its stagnation point on the dawn-dusk meridian, the McIlwain field does not, again exhibiting a deformed bulge region with the stagnation point somewhere on the nightside (caused by the rotation away from a noon-midnight symmetry axis). These are nonclassical trajectory maps, but they better match the ion distributions deduced from high-energy neutral atoms observed by the detectors on the IMAGE spacecraft (D. Mitchell, personal communication, 2000). In addition, they are more in line with particle trajectories through more sophisticated potential pattern calculations [cf. *Sojka et al.*, 1986; *Papitashvili et al.*, 1994; *Weimer*, 1996; *Weiss et al.*, 1997; *Garner*, 2000; *Fok et al.*, 2001]. Note that *Korth et al.* [1999] found that a Volland-Stern field provides a good description of the access of particles to geosynchronous orbit. The McIlwain field will have similar agreement because the pattern at this radial distance is very similar to the Volland-Stern description. The improvement provided by the McIlwain description is in the region inside of this altitude.

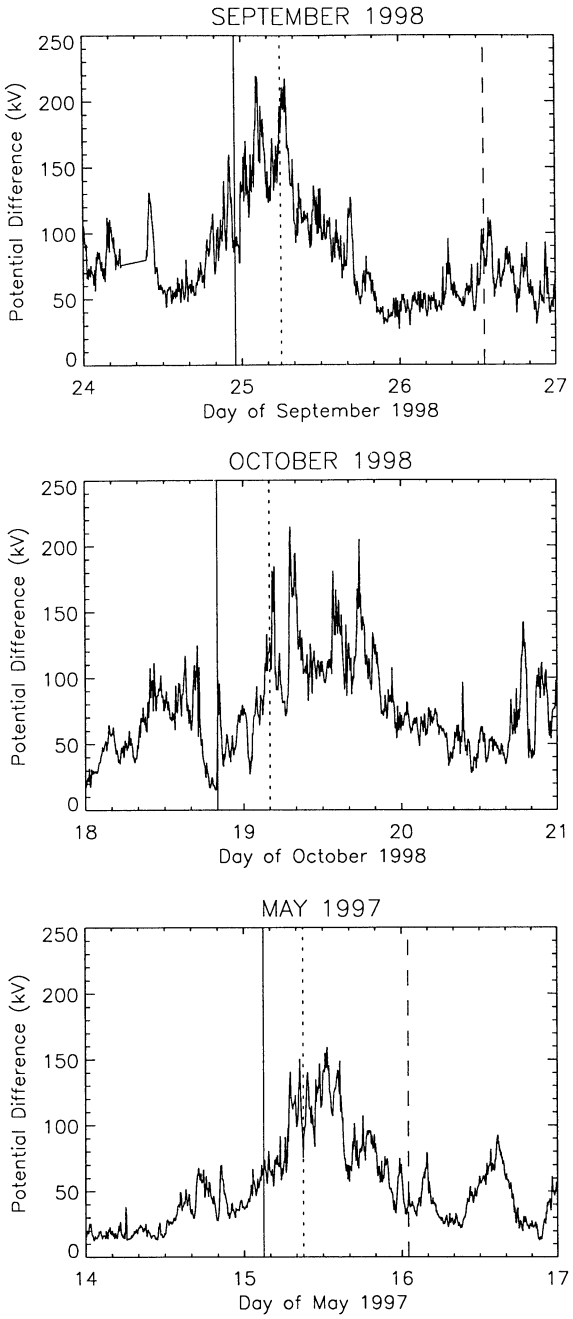

Figure 7. Cross-polar cap potential differences for the three storms as calculated by the AMIE model. Vertical lines are the same as in Figure 1, marking the times of the shock arrival and the leading and trailing edges of the CME.

For the storm simulations discussed in this study, the driver for the McIlwain field will be the cross-polar cap potential ($\Delta\Phi_{pc}$) calculated from the assimilative mapping of ionospheric electrodynamics (AMIE) model [*Richmond and Kamide*, 1988]. The width of the magnetosphere, which is needed in (12) to convert this potential into an electric field, is found using the *Shue et al.* [1998] magnetopause description. This formula yields a very reasonable shape and location of this boundary during quiet and active times [*Shue et al.*, 1998, 2000]. This provides a high-resolution representation of the electric field strength, based on solar wind drivers as well as the ground-based and satellite data included in the AMIE calculation. These values of $\Delta\Phi_{pc}$ are shown in Figure 7. Note the differences between $\Delta\Phi_{pc}$ for the three storms. The September 1998 storm has a long period of high $\Delta\Phi_{pc}$ (early on September 25), the October 1998 storm has a much longer interval of slightly lower $\Delta\Phi_{pc}$ (most of October 19), while the May 1997 storm has a shorter interval of even smaller $\Delta\Phi_{pc}$ as its maximum convection strength. These differences will be important in the development of the stormtime *Dst**.

5. Modeling Results

In order to quantify the contribution to *Dst** from each component (symmetric and asymmetric) of the ring current, the accuracy of the model in reproducing *Dst** will be examined. Figure 8 shows the observed *Dst** value against a similar model quantity calculated from the total ring current energy according to the Dessler-Parker Sckopke equation [*Dessler and Parker*, 1959; *Sckopke*, 1966],

$$Dst^*[\mathrm{nT}] = -\frac{E_{RC}[\mathrm{keV}]}{2.51\times10^{29}} \tag{16}$$

which relates the total energy in the ring current E_{RC} to the average magnetic field depression at the Earth. Note that the modeled value is the sum of the H^+ and O^+ energy integrals. Three curves are shown in each frame: the observed *Dst** profile (*Dst* with magnetopause currents and the Earth's diamagnetic effects (a factor of 1.3 was used) removed), the modeled *Dst** from (16) from a simulation using the Volland-Stern convection field, and the modeled value using the McIlwain field. September 1998 has the best agreement between the modeled and measured *Dst**. October 1998 is also not far off, although the second decrease in *Dst** is not captured by the simulation. The comparison for May 1997 is not particularly close, although the shape is similar.

As mentioned in the Introduction, the DPS relation only considers the perturbation from $\mathbf{J}_\perp$, and the effects of the partial ring current closure current system are neglected by (16). A full investigation of the influence of these other segments of the current loop is beyond the scope of this study but will be considered in the near future.

Examination of MPA observations during the second *Dst** minimum during the October 1998 storm reveals that the satellite observed several abrupt density dropouts throughout this interval. This is seen in both the nightside (Figure 2) and dayside (Figure 3) measurements. This behavior is most likely the result of magnetic field reconfigurations shifting plasma sheet away from the satellite location. Therefore, using only the relative maxima at the beginning of each of these dropout features is a better representation of the true nightside plasma sheet density. Such a density profile is shown in Figure 9 (top). Note that the only changes from Figure 2 are from 0800 UT to 2000 UT on October 19. Also shown in Figure 9 (bottom) is a comparison of the *Dst** from a simulation with this new MPA input file. It is seen that the second *Dst** minimum is now replicated quite well by the simulation results. This difference in model results highlights the need to accurately know the near-Earth nightside plasma sheet density in order to simulate the hot ion flow through the inner magnetosphere. The simulation results using the "filled-in" boundary condition for the October 1998 storm will be used hereafter for all plots of this storm.

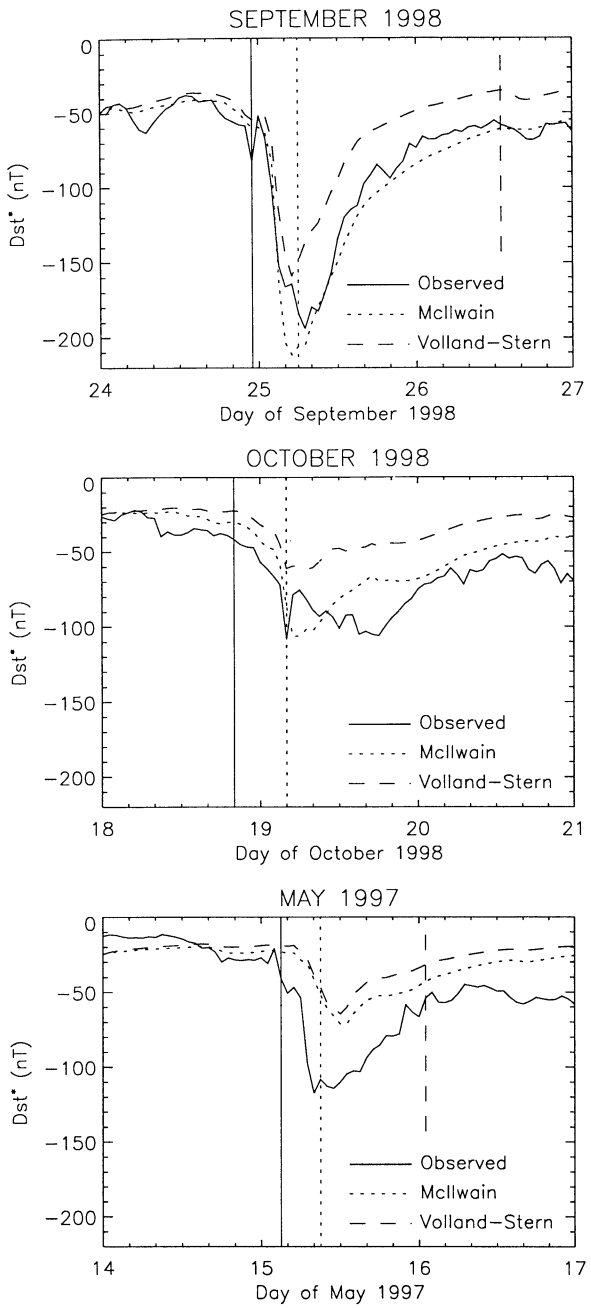

Figure 8. Observed *Dst** (solid lines) and the simulated *Dst** from the two field descriptions (McIlwain, dotted line; Volland-Stern, dashed line) for the three storms. Vertical lines are the same as in Figure 1, marking the times of the shock arrival and the leading and trailing edges of the CME.

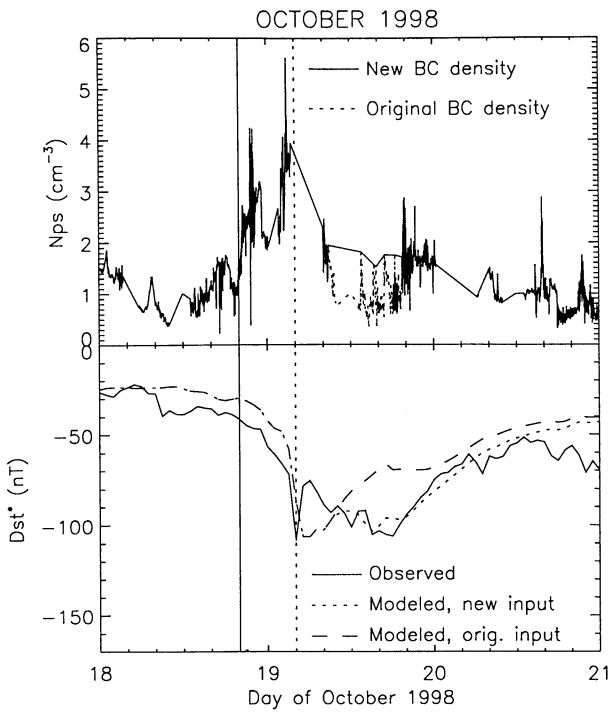

Figure 9. (top) Nightside plasma sheet density and (bottom) *Dst** showing the difference achieved by filling in the density dropouts in the boundary condition (BC) from 0800 to 2000 UT on October 19. Model runs are with the McIlwain electric field description. Vertical lines are the same as in Figure 1, marking the times of the shock arrival and the leading and trailing edges of the CME.

Discrepancies between the observed and modeled *Dst** values are expected, though. Recent studies have found that the ring current may only account for a portion (albeit a major one) of the observed *Dst**, because of the other current systems mentioned above. For instance, ring current observations have shown that only 40%-70% of the *Dst** value can be accounted for by the ion energy [e.g., *Roeder et al.*, 1996; *Greenspan and Hamilton*, 2000]. One possible source of additional perturbation is the tail current sheet. *Alexeev et al.* [1996] found that ~30% of the *Dst** can be accounted for by the magnetotail current sheet, and *Turner et al.* [2000] found that the tail currents can account for ~25% of the *Dst** value. In the present study, all particles within the simulation boundary are counted in the total energy integral (out to 6.625 R_E, the outer boundary of the last grid cell), whether they contribute to a symmetric ring current, partial ring current, or tail current. Another effect that is not included in the model is the modification to the magnetic field by the ring current itself (called the ring current self-field). The effect of the ring current self-field on *Dst** is to produce a 5-35% larger decrease for the same total energy [*Carovillano and Siscoe*, 1973]. On the other hand, because the self-field decreases the total field, it also repels ions from the inner magnetosphere through conservation of the third adiabatic invariant. Therefore it is uncertain what the self-consistent influence of this field will be on *Dst**. Externally driven compressions and expansions of the magnetosphere (as are caused by solar wind changes and substorms) should cause even bigger energization changes in *Dst** as a result of the adiabatic response of the ring current [cf. *Fok et al.*, 1996; *Fok and Moore*, 1997]. Regardless of these caveats, the simulation results will be used in their present form.

Note that the modeled *Dst** for the Volland-Stern field shown in Figure 8 for the September 1998 storm is less than that from a simulation of the same event reported by *Liemohn et al.* [1999]. In the study by *Liemohn et al.* [1999] the simulated *Dst** was scaled so the prestorm *Dst** value was the same as the observed value. However, in the present study, the initial condition was enhanced to match the prestorm values, and no scaling was applied to the rest of the *Dst** profile. Second,

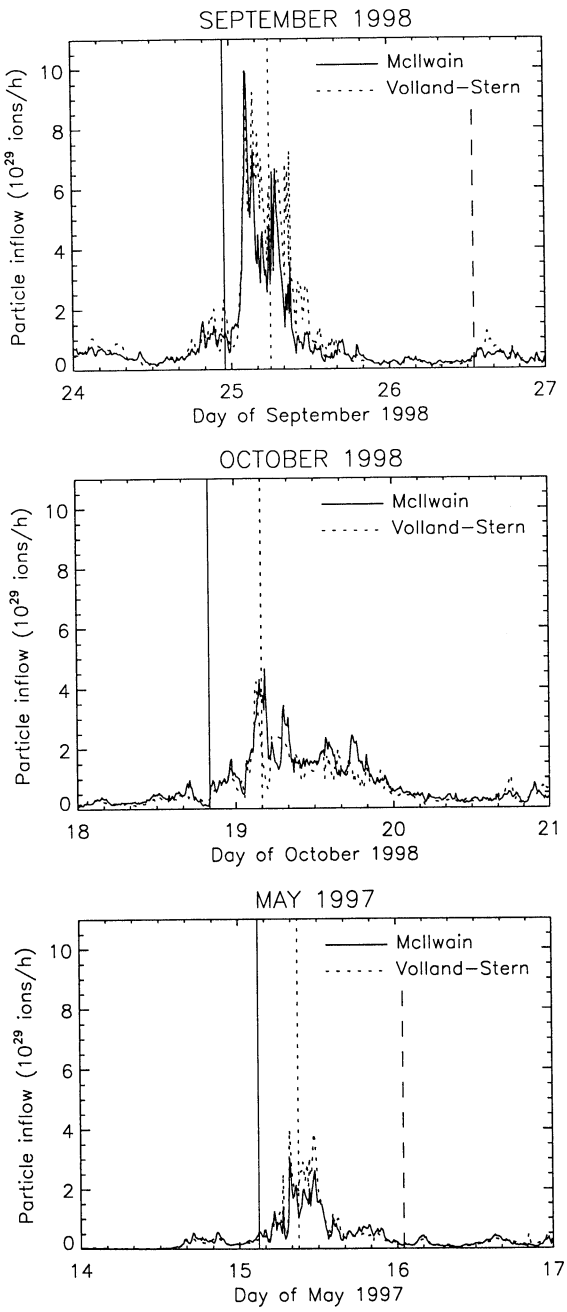

Figure 10. Particle inflow rate during the three storms for the two field descriptions (McIlwain: solid line; Volland-Stern: dotted line). Vertical lines are the same as in Figure 1, marking the times of the shock arrival and the leading and trailing edges of the CME.

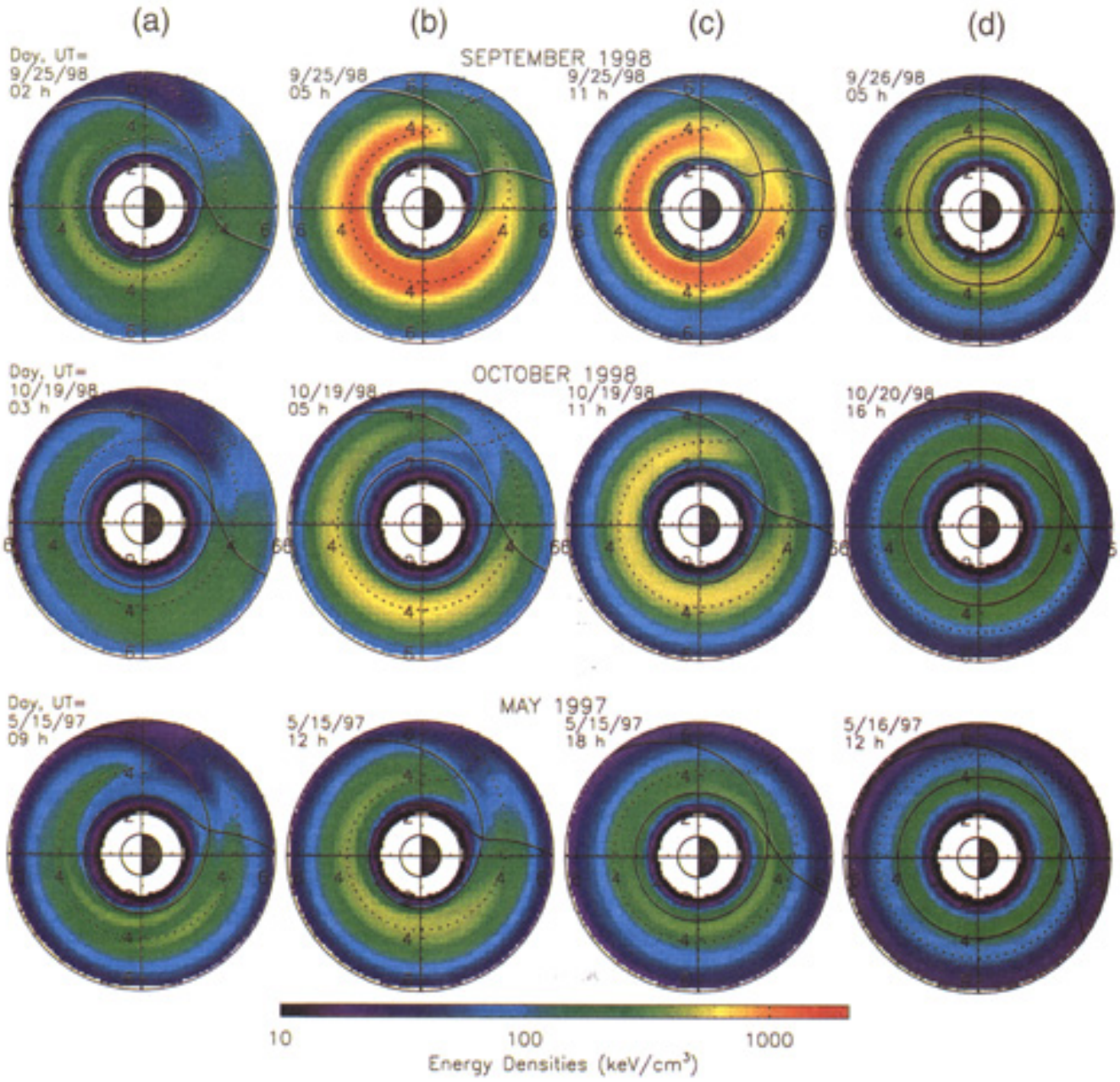

Plate 1. Equatorial plane energy density of the simulated ring current (McIlwain field description, summed H^+ and O^+) at four times: (a) growth phase, (b) storm peak, (c) early recovery, and (d) late recovery during the three storms in (top) September 1998, (middle) October 1998, and (bottom) May 1997. Note that the color scale is logarithmic. The solid and dotted lines are the $E_{6.6}$=3 and 12 keV last closed drift trajectories, respectively.

the plasma boundary condition has been refined somewhat using information at local times closer to dawn and dusk to fill in gaps in the satellite coverage. Last, higher time resolution is achieved in the electric field and plasmasphere models using the MBI-derived *Kp* profile, which refines the timing and intensity of the injection sequence. The small resulting differences do not alter our previous study's main conclusion: dayside outflow is far bigger than charge exchange as a loss mechanism during the early-phase decay of the ring current. This finding is confirmed in the results presented below.

In all three plots of Figure 8 the McIlwain field produced a larger total ring current energy than the Volland-Stern field. A question to ask then is whether this increase is caused by enhanced nightside inflow or deeper penetration of flow trajectories into the inner magnetosphere. Figure 10 presents the particle inflow rate across the nightside outer boundary of the model for the two electric field models for each storm. This inflow rate is calculated by integrating the total flux of particles through the nightside outer simulation boundary. It is clear that the inflow rates are very similar between the field models. In fact, the inflow is higher in each event for the Volland-Stern model than for the McIlwain model. This implies that the deeper *Dst** minimum using the McIlwain field is due to particles drifting closer to the Earth.

Figure 10 also illustrates the difference between the three storms in particle inflow. Because of the much stronger activity level (and hence the scaled convection electric field) of September 1998, this storm had much higher particle inflow values than the other two storms. May 1997 is particularly weak, and the lack of a substantial *Dst** depression from the simulated ring current is directly related to this weak particle influx.

It is useful to examine more closely the spatial energy distribution in the ring current with respect to open and closed drift path boundaries. Plate 1 shows the equatorial plane energy density (combined H^+ and O^+) at four times during each storm (during the initial drop in *Dst**, at the modeled *Dst** minimum, 6 hours later during the fast recovery, and then in the late recovery phase). Note that these results are from the McIlwain field simulation results. Overlaid on each plot is the

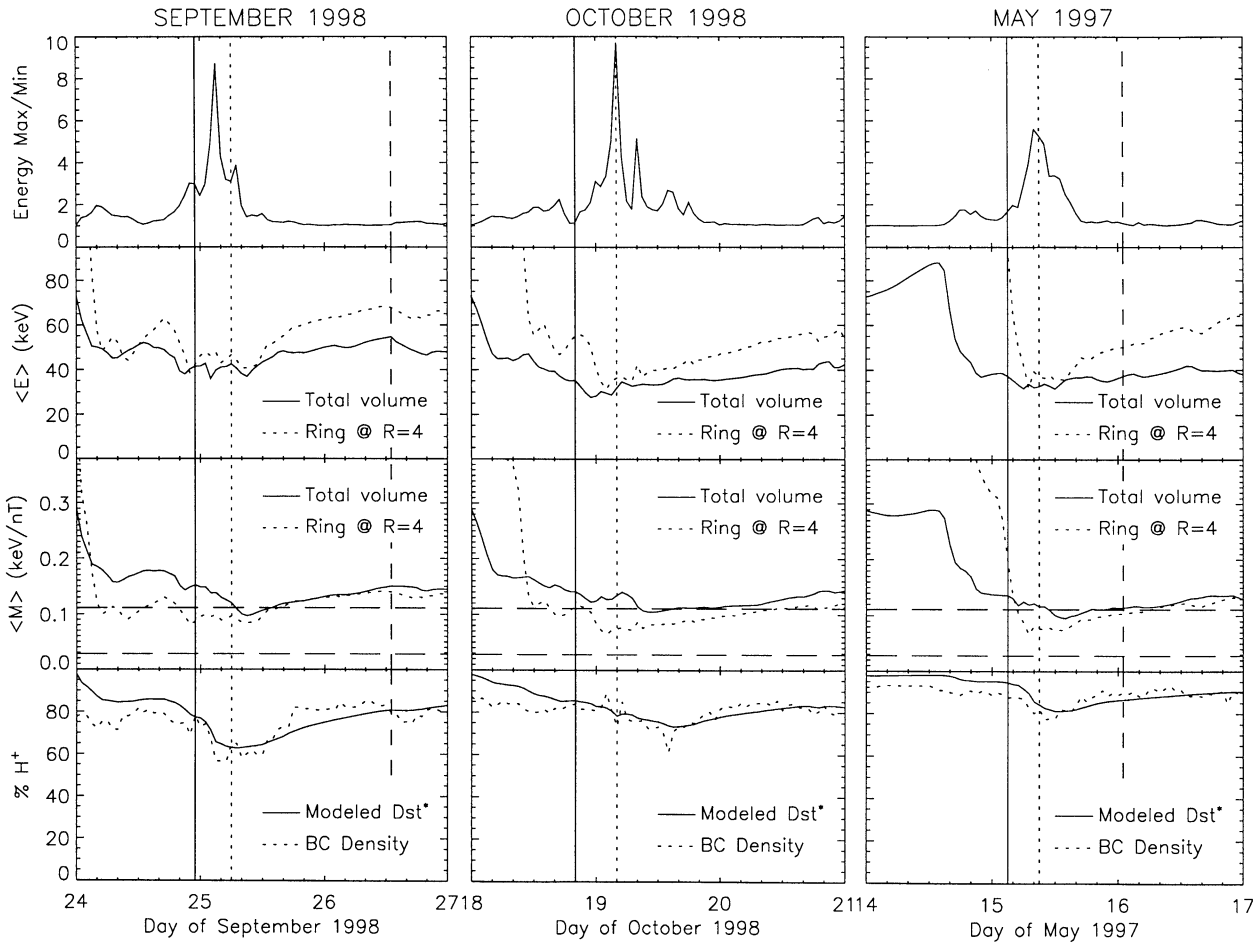

Figure 11. Bulk quantities from the 3 storms (each column, as in Figure 1) for the McIlwain simulation results. (top row) Ratio of the maximum-to-minimum values of the radial integral of the equatorial plane energy density (from Figure 8). (second row) Average energy of the ring current ions (solid line) and the average energy from the MPA portion of the boundary condition (dotted line). (third row) Average adiabatic invariant

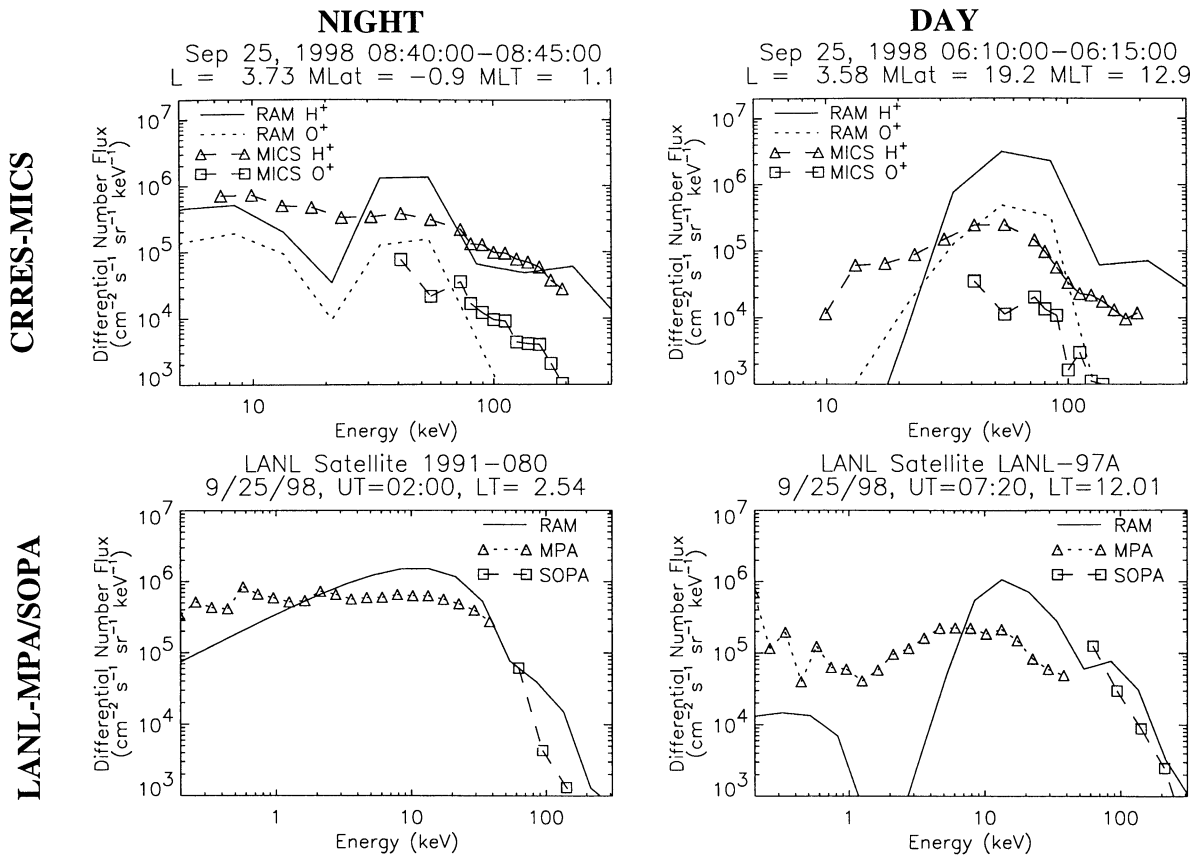

Figure 12. (top) Energy spectra comparisons between the McIlwain simulation results and Polar-MICS observations and (bottom) LANL MPA and SOPA observations on the (left) nightside and on the (right) dayside. The MICS comparisons are of locally mirroring particles for each ion species, while the LANL comparisons are pitch angle averaged fluxes summed over species. Exact times and locations are shown above each plot.

last closed trajectory for ions of $E_{6.6}$=3 keV (solid line) and 12 keV (dotted line). It is seen that these separatrices contract and expand as activity changes, and in fact the $E_{6.6}$=12 keV boundaries are entirely outside of the simulation domain in the right-hand plot for all 3 storms.

There are several very striking features in Plate 1. One is that the main phase ring current is highly asymmetric in local time, with a peak intensity located postdusk and a clear minimum predawn. This asymmetry is very intense, and can be quantified by examining radial integrals of the plasma energy density as a function of local time. The top row of Figure 11 shows that the maximum-to-minimum ratio of this local time asymmetry exceeds 5 for all three storms (see Figure 11, top row). Large asymmetries persist through the early recovery phase of the storms, and the distribution does not relax into a classical symmetric ring current until late in the recovery phase.

Another feature of Plate 1 is that, during the storm peak, the bulk of the ring current energy is located just beyond the $E_{6.6}$=3 keV boundary (in other words, on open drift paths). This is consistent with the average energy of the modeled ring current, shown in Figure 11 (second row). Two values are plotted, the average energy for the entire simulation domain and the average energy of the ring at R=4 (roughly at the peak of the stormtime ring current). The energy begins quite high (the average energy of the initial condition), drops once the storm begins, and then slowly rises after the storm. The average energy is ~40 keV for all three storms during the main phase. The rise after the storm is because the low-energy ions are preferentially lost from the system. Also shown in Figure 11 (third row) is the average first adiabatic invariant value of the simulated ring current (again, for the entire volume and for a ring at R=4), along with the M values of $E_{6.6}$=3 and 12 keV (horizontal dashed lines) for reference. The entire volume $\langle M \rangle$ reaches a minimum below the $M(E_{6.6}$=12 keV) value very soon after the *Dst** minimum for all three storms. The R=4 $\langle M \rangle$ has a lower minimum value at a slightly earlier time, roughly at the storm peak. The similarity of the minimum value with the average energy of the injection (which is between the two dashed lines) indicates that most of the ions at this time are freshly injected from the tail. This fact, combined with the asymmetry of the spatial pattern in the modeled ring current seen in Plate 1 and the top row of Figure 11, implies that most of the main phase *Dst** is from the partial ring current, in agreement with the conclusions of previous studies [*Takahashi et al.*, 1990; *Liemohn et al.*, 1999; *Grafe*, 1999]. A more quantitative examination of this is presented in the next section.

To quantify how well the model reproduces the satellite observations, simulated spectra are compared to observations at selected locations. For conciseness, only September 1998 will be discussed in this context. Such comparisons are shown in Figure 12, with Polar-MICS (top) and with the LANL MPA and SOPA observations (bottom). The two MICS comparisons

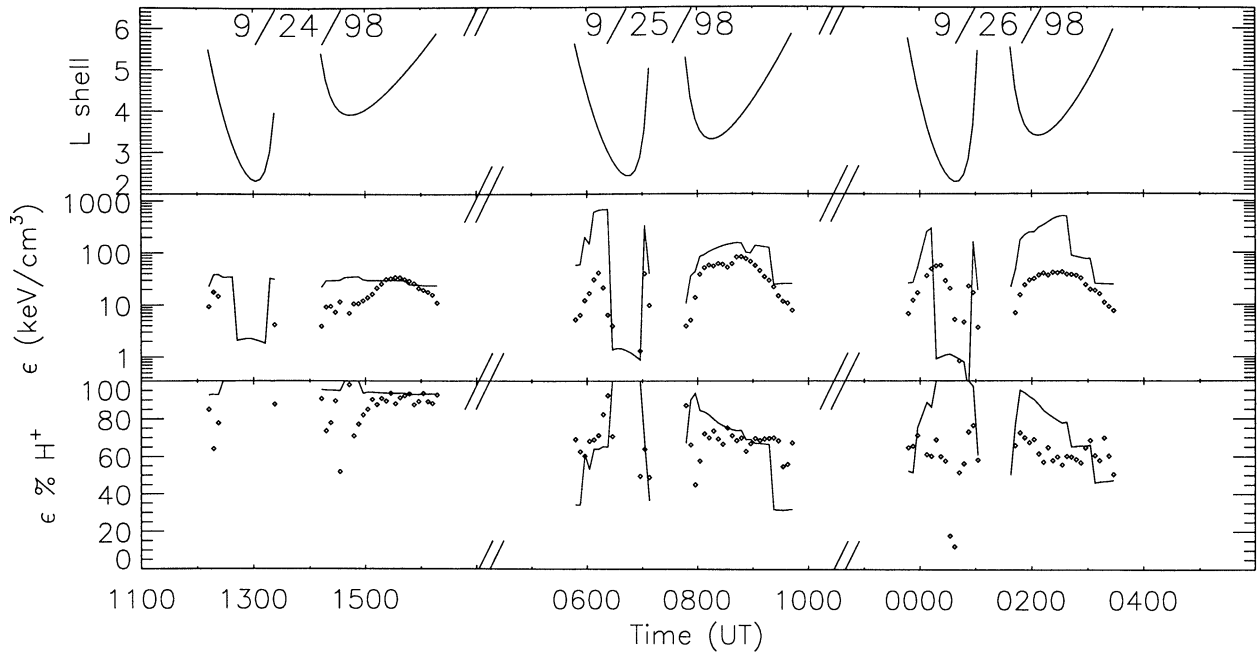

Figure 13. (middle) Energy density and (bottom) percent H^+ contribution to this value between the Polar-MICS observations (symbols) and the McIlwain simulation results (solid lines). (top) Also plotted is the *L* shell of the satellite during the three orbits, as in Figure 3.

are energy spectra seen near the equatorial plane for a northbound (nightside) pass and the preceding southbound (dayside) pass of the satellite through the inner magnetosphere during the early recovery of the storm. Shown are H^+ and O^+ locally mirroring spectra from the instrument and from the model results using the McIlwain field. As in Figure 4, only the high-energy mode from the MICS instrument is shown. It is seen that reasonable agreement is achieved, especially on the nightside. The model overpredicts the H^+ distribution somewhat and underpredicts the $E<20$ keV ions, especially on the dayside. The agreement for O^+ is better, although the model also overpredicts the fluxes for this species for this storm.

The comparisons with the LANL spectra (Figure 12, bottom) show a similar trend, with good agreement on the nightside (as expected), and reasonable agreement on the dayside. Disagreement on the nightside is because the moments of the distribution function are used in the boundary condition and also because multiple satellites are used to construct the boundary condition. Note that these spectra are pitch angle-averaged results summed over all ion species. Again, it is seen that the model underpredicts the low-energy distribution on the dayside. Because these low-energy particles are more sensitive to the convection flow pattern (because gradient-curvature drifts are energy dependent), the choice of a non-self-consistent magnetospheric electric field is most likely responsible for this discrepancy.

Another in situ data comparison is presented in Figure 13, again for the September 1998 storm, analogous to Figure 4. The top panel shows the *L* shell location of the Polar satellite for each orbit (as shown in Figure 4). Shown in the middle panel is local energy density, integrated from the phase-space distributions for $E\geq30$ keV, from the MICS observations (symbols) and from the model results (solid lines). It is seen that the energy densities from the model are quite similar to the values from MICS and tend to be higher when there is a difference. In the lower panel of Figure 13 is the percent contribution to this energy density from H^+ (again, for the observations and the simulation results). The agreement is quite good throughout the storm sequence, although September 26 is less good. This indicates that the choice of composition at the boundary is acceptable. This species breakdown is seen in Figure 11 (bottom) for the three storms, showing the *Young et al.* [1982] H^+ density percentage as well as the total contribution of H^+ to the modeled *Dst** value. The empirical formulas of *Young et al.* [1982] predict a minimum H^+ concentration of 59%, 71%, and 80% for the three storms, with H^+ occasionally exceeding 95% of the boundary condition density. It is seen that the boundary value composition dictates the overall composition, with some response time lag as the particles are lost from the system (through outflow, charge exchange, or precipitation).

Given the excellent agreement between the observed and simulated *Dst** (Figure 8), the overprediction of the ring current fluxes is expected. As stated previously, spacecraft observations indicate that not all of the *Dst** can be accounted for by measured ion fluxes. The balance is due to the ring current self-field or non-ring-current systems. Potential sources of error in the simulation include spatial versus temporal ambiguity in the satellite observations used for the outer boundary condition, and lack of self-consistency in the global electric field model. In addition, the partial ring current closes along field lines and through the ionosphere. This will have some net effect on the *Dst* value, most likely in the positive direction [*Siscoe and Crooker*, 1974]. Similarly, the omission of an explicitly defined penetration electric field and/or time-varying magnetic field effects (causing radial diffusion [*Chen et al.*, 1994; *Fok et al.*, 1996]) limit the validity of the simulation results. *Dst** discrepancies could also be because the LANL satellites did not measure one or more high-density injections of plasma during the October 1998 and May 1997

storms. In any case, the simulated ring current replicates many of the features of the observed one, and this validates an analysis of the stormtime ring current based on these modeled distributions.

6. Contributions to *Dst** From Particles on Open or Closed Trajectories

A rigorous analysis of the contributions to *Dst** from the symmetric and partial ring currents requires that the open-closed drift path status of each phase space grid cell at each timestep be determined. However, to reduce this computationally impractical calculation to a tractable level, trajectories were calculated for half of the energy cells for a quarter of the radial grid cells (those on the integer L shells) every third azimuthal spatial step (every 3 hours LT). This was done once an hour throughout the simulations. The goal of this calculation is to determine the instantaneous open-closed status of the particles, rather than the final fate of the particles in that phase-space cell, because this status is related to the partial ring current magnitude at that specific universal time. Therefore the convection pattern is assumed static for each trajectory calculation, determined by the instantaneous geophysical parameters. Please note that in referring to open or closed drift paths in the following discussion, it is the instantaneous value of this status that is being cited, and the open-closed status of any particular ion can change as it moves through the simulation domain. The drift paths were found by solving (4), (11), (13), and (14) using a fourth-order Runge-Kutta method [e.g., *Press et al.*, 1992]. A trajectory was said to be closed if it reached $\pm 2\pi$ from its initial azimuthal position, or if it remained within the simulation domain for more than 24 hours.

Figure 14 shows the results from such a calculation for each of the three storms (from the simulations with the McIlwain field). The value plotted is the percent contribution to the modeled *Dst** value from particles on instantaneously open drift paths. In all three storms, it is seen that this number is initially very low. As the storm develops, the contribution from the partial ring current increases, eventually reaching a maximum above 80% near the storm peak. It then recedes back to its prestorm level (<20%) in the late recovery phase. Comparing Figure 14 with Figure 7, it is seen that the contribution from the partial ring current is highly dependent on the convection strength. As $\Delta\Phi_{pc}$ increases, the convection increases. This reduces the size of the separatrices, and thus more of the ions in the inner magnetosphere are classified as being on open drift paths. Therefore much of the same structure of Figure 7 is seen in Figure 14, although Figure 14 combines an integrated time history of the convection strength, source intensity, and loss processes. Also, remember that Figure 14 has values every hour while Figure 7 has values every 5 min. Comparing Figure 14 with Figure 8 reveals that the peak in partial ring current contribution occurs just before the *Dst** minimum. This is also expected because, at the *Dst** minimum, the sources and losses are balanced and the ring current drivers (particularly the boundary condition flux) are already beginning to wane.

The comparison between Figures 7 and 14 requires additional discussion. The oscillations in the convection strength, as governed by $\Delta\Phi_{pc}$ from Figure 7, do not necessarily reconfigure the ring current from asymmetric to symmetric on the timescales of the changing electric field. Rather, only the open-closed drift boundaries are changing, and the spatial

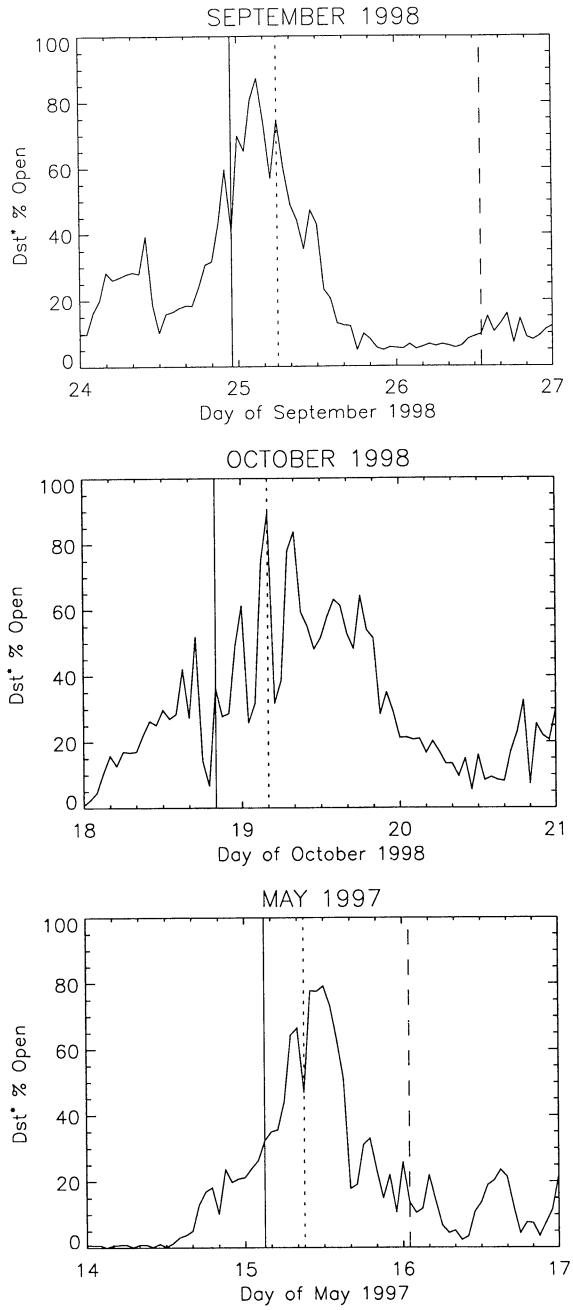

Figure 14. Percent contribution to the calculated *Dst** index from the McIlwain field simulations from particles on open drift paths. Vertical lines are the same as in Figure 1, marking the times of the shock arrival and the leading and trailing edges of the CME.

profiles themselves remain asymmetric during the main phase of the storms. The results shown in Figure 14 could therefore be construed as a minimum contribution to *Dst** from the partial ring current, because the contribution from the ions on closed drift paths may also have a dawn-dusk asymmetry. A full calculation of the symmetric and partial ring current system from these plasma simulation results is beyond the scope of this study but is planned for the near future.

To better understand the contribution to *Dst** from particles on open or closed drift paths, it is useful to consider the percentage of plasma energy on open drift paths as a function of

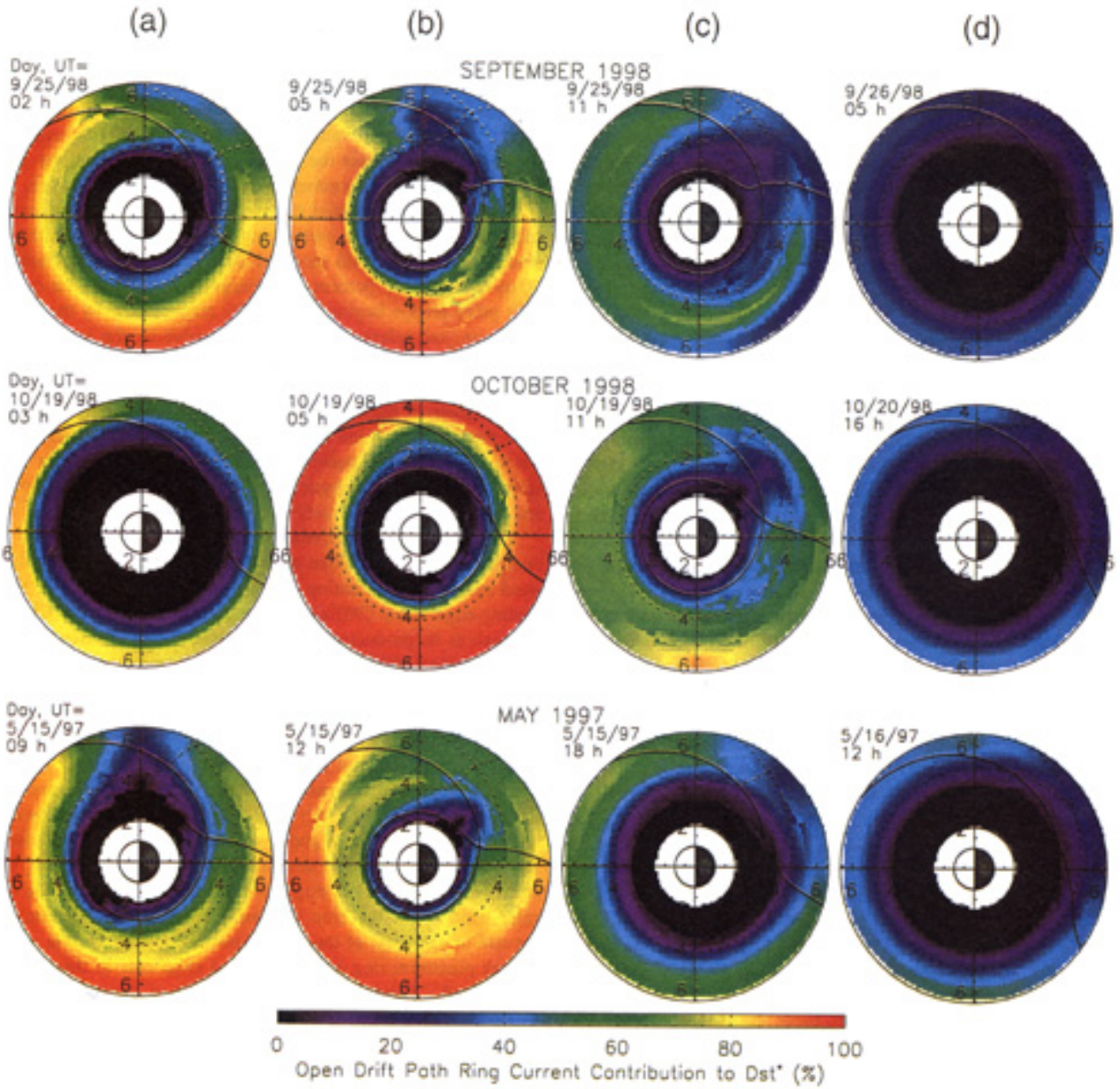

Plate 2. Dial plots (like Plate 1) of the percent contribution to the local ion energy density from particles on open drift paths. Times are the same as in Plate 1. Note the color scale is linear. The solid and dotted lines are the $E_{6.6}$=3 and 12 keV last closed drift trajectories, respectively.

spatial location. Plate 2 shows dial plots of this percentage as a function of spatial location at four times during the storm (the same times as shown in Figure 10: growth phase, storm peak, initial recovery, and late recovery). Also, as in Figure 10, the separatrices for $E_{6.6}$=3 and 12 keV are shown (solid and dotted lines, respectively) for reference. It is seen that much of the duskside stormtime ring current is on open drift paths. Conversely, the near-Earth predawn sector remains dominated by ions on close drift paths. This was qualitatively inferred from Figure 10 and is shown quantitatively here. The combination of the energy densities in Figure 10 with the percentage of that value on open drift paths shown in Plate 2 gives the relative contribution of each spatial location to the total value shown in Figure 14. Because the stormtime peak in energy density is near dusk and the predawn sector has relatively low energy densities, the integrated result is that most of the ring current energy (and therefore *Dst**) is from particles on open drift paths. Again, these percentages should be treated as a minimum contribution when discussing symmetric and asymmetric ring current contributions, because even the closed drift path distributions could be (and, during the main phase, mostly are) nonuniform around the Earth.

It should be noted that the compositional bias towards H^+ (seen in Figures 11, 12, and 13) removes the possibility that the initial recovery of the storm is due to charge exchange of O^+ with the geocorona, as confirmed by *Liemohn et al.* [1999]. This is particularly true for the September 1998 storm, where the initial recovery was very fast and the *Dst** was well modeled. Examination of E_y from Figure 1, N_{ps} from Figure 2, and $\Delta\Phi_{pc}$ from Figure 7 shows that the ring current source term often drops off long before the convection strength drops. Figure 3 confirms that the dayside outflow also cuts off when the nightside density decreases. During this high-convection yet low-plasma-sheet-density interval, most of the initially injected high-density plasma is replaced with freshly injected low-density plasma. Not coincidentally, this is during the early recovery phase of the storms (see Figure 8). This is seen in Plate 2 (third column) as the open drift path contribution on the duskside remains above 50%, indicating flow-through is an important process at this storm phase. While this spatial region still has the highest open drift path percentage, it is not as high as during the main phase of the storm for two reasons: (1) the convection strength is dropping, so the highest and lowest energy particles are being captured on closed drift paths; and (2) the open trajectories (middle energies) are being quickly filled with low-density plasma, thus contributing less to the total energy density at these locations. It is not until late in the storm recovery that charge exchange becomes the dominant process in decreasing the ion total energy content.

7. Conclusion

Three storms with similar solar wind driver structures from the same period of the solar cycle were examined to determine the contribution to the *Dst* index from the symmetric and asymmetric (partial) components of the ring current, as proxied by the amount of plasma energy carried by particles on open or closed drift paths. It was found, through analysis of both observations and theoretical modeling results, that at the peak of all three storms, most of the ion energy content in the inner magnetosphere (and through (16) also *Dst**) is from particles on open drift paths (the partial ring current). While there are regions of near-Earth space, such as the predawn sector inside of R=4, that have an energy content that is always dominated by ions on closed drift paths (symmetric ring current particles), the energy density of this region is far lower (by a factor of 5 to 10) compared to that on the duskside, where nearly all of the trajectories are open. This open drift path dominance crests and ebbs with the strength of the convection electric field, primarily controlled by the cross-polar cap potential difference. Late in the storm recovery phase, when convection has diminished and the newly captured ions have begun to spread in azimuth around the Earth, particles on closed drift paths dominate the *Dst** contribution. It is noted that the calculated percentages of particles on open drift paths serves as a minimum value for the percentage of ring current that is partial, because the closed drift path distributions are often also spatially asymmetric during geomagnetic storms.

It should be emphasized that the low-high-low percent contribution profile for the partial ring current is true for all three storms examined. With modeled *Dst** minima ranging from -70 to -210 nT, the percent ion energy from particles on open drift paths always begins below 10%, reaches 80% by the *Dst** minimum, and relaxes to the prestorm value by the late recovery phase. The major contribution to the open drift path energy integral is from the afternoon and dusk region, with the outer L shells at these local times always maintaining at least 30% open drift path ion energy. The consistency between the storms leads to the generalization that this is true for all storms with these geophysical and solar wind driver functions and profiles, and most likely it is true for storms in general.

Three main geoeffectiveness issues are highlighted by a comparison of these three events. First, the shocked solar wind structures (containing strong southward IMF B_z) at the leading edge of the CMEs are more geoeffective than the CMEs themselves in producing *Dst** decreases during the September 1998 and May 1997 storms. This was not true for the October 1998 storm, however. The solar wind sheath preceding the October 1998 CME did not contain significant southward IMF B_z and therefore it was not geoeffective. The *Dst** profile for this event was different than for the other two storms, with a much more gradual decrease associated with the CME arrival rather than with the sheath. Second, the interval of time with high convection strength and low nightside plasma sheet density must be examined in determining the geoeffectiveness of solar wind structures on ring current decay. The magnitude of solar wind E_y and the drop in plasma sheet density determine the rate of exchange of the strong stormtime ring current with a weak poststorm ring current. Such a swap aids in the recovery of *Dst**. Third, the duration and rate of change in solar wind E_y at the trailing edge of the CME is another factor that determines the duration and characteristic timescales for the early recovery phase of the storms. The rate of E_y decrease directly corresponds to the clarity of the two-phase decay signature as convection is switched off. This important geoeffective element has not been previously considered.

Several other issues were also discussed in this study. It was shown that the McIlwain electric field description with a $\Delta\Phi_{pc}$ driver can be used to create a reasonable ring current in the inner magnetosphere. It was also shown that the fast decay of the ring current during these storms is caused by dayside outflows. The lack of much O^+ injected into the inner magnetosphere prevents its charge exchange from being the main loss process during this interval of the storms. It was demonstrated that the observed *Dst** value is not created solely by the ring current, because observed ion fluxes are overpredicted when

this is the case. Finally, it was shown that E_y alone is not enough to predict the rise or fall of *Dst**, but other factors must also be included, such as N_{sw} and the timing and sequence of the driver functions with respect to one another.

Acknowledgments. This work was supported by NASA grant NAG5-4771 and NSF contracts ATM-9711381 and ATM-9800830. The MBI was provided by the USAF Research Laboratory, Hanscom AFB, MA, the solar wind and IMF data from the WIND spacecraft are from the CDAWeb ITSP Key Parameter database, and the Kp and *Dst* indices are from the Kyoto World Data Center-C2 in Kyoto, Japan.

Janet G. Luhmann thanks referees for their assistance in evaluating this paper.

References

Akasofu, S.-I., Energy coupling between the solar wind and the magnetosphere, *Space Sci. Rev., 28*, 121, 1981.

Alexeev, I. I., E. S. Belenkaya, V. V. Kalegaev, Y. I. Feldstein, and A. Grafe, Magnetic storms and magnetotail currents, *J. Geophys. Res., 101*, 7737, 1996.

Baumjohann, W., G. Paschmann, and C. A. Cattell, Average plasma properties in the central plasma sheet, *J. Geophys. Res., 94*, 6597, 1989.

Belian, R. D., G. R. Gisler, T. Cayton, and R. Christensen, High-Z energetic particles at geosynchronous orbit during the great solar proton event series of October 1989, *J. Geophys. Res., 97*, 16,897, 1992.

Bilitza, D., International reference ionosphere: Recent developments, *Radio Sci., 21*, 343, 1986.

Birn, J., M. F. Thomsen, J. E. Borovsky, G. D. Reeves, D. J. McComas, and R. D. Belian, Characteristic plasma properties during dispersionless substorm injections at geosynchronous orbit, *J. Geophys. Res., 102*, 2309, 1997.

Bittencourt, J. A., *Fundamentals of Plasma Physics*, Pergamon, New York, 1986.

Borovsky, J. E., M. F. Thomsen, and D. J. McComas, The superdense plasma sheet: Plasmaspheric origin, solar wind origin, or ionospheric origin?, *J. Geophys. Res., 102*, 22,089, 1997.

Borovsky, J. E., M. F. Thomsen, and R. C. Elphic, The driving of the plasma sheet by the solar wind, *J. Geophys. Res., 103*, 17,617, 1998a.

Borovsky, J. E., M. F. Thomsen, D. J. McComas, T. E. Cayton, and D. J. Knipp, Magnetospheric dynamics and mass flow during the November 1993 storm, *J. Geophys. Res., 103*, 26,373, 1998b.

Burton, R. K., R. L. McPherron, and C. T. Russell, An empirical relationship between interplanetary conditions and *Dst*, *J. Geophys. Res., 80*, 4204, 1975.

Campbell, W. H., Geomagnetic storms, the *Dst* ring-current myth and lognormal distributions, *J. Atmos. Terr. Phys., 58*, 1171, 1996.

Carovillano, R. L., and G. L. Siscoe, Energy and momentum theorems in magnetospheric processes, *Rev. Geophys., 11*, 289, 1973.

Carpenter, D. L., and R. R. Anderson, An ISEE/whistler model of equatorial electron density in the magnetosphere, *J. Geophys. Res., 97*, 1097, 1992.

Chappell, C. R., K. K. Harris, and G. W. Sharp, The morphology of the bulge region of the plasmasphere, *J. Geophys. Res., 75*, 3848, 1970.

Chappell, C. R., K. K. Harris, and G. W. Sharp, The dayside of the plasmasphere, *J. Geophys. Res., 76*, 7632, 1971.

Chen, M. W., L. R. Lyons, and M. Schulz, Simulations of phase space distributions of storm time proton ring current, *J. Geophys. Res., 99*, 5745, 1994.

Chen, J., T. A. Fritz, R. B. Sheldon, H. E. Spence, W. N. Spjeldvik, J. F. Fennell, S. Livi, C. T. Russell, J. S. Pickett, and D. A. Gurnett, Cusp energetic particle events: Implications for a major acceleration region of the magnetosphere, *J. Geophys. Res., 103*, 69, 1998.

Crooker, N. U., and A. H. McAllister, Transients associated with recurrent storms, *J. Geophys. Res., 102*, 14,041, 1997.

Daglis, I. A., E. T. Sarris, and B. Wilken, AMPTE/CCE observations of the ion population at geosynchronous altitudes, *Ann. Geophys., 11*, 685, 1993.

Dessler, A. J., and E. N. Parker, Hydromagnetic theory of geomagnetic storms, *J. Geophys. Res., 64*, 2239, 1959.

Ebihara, Y., and M. Ejiri, Modeling of solar wind control of the ring current buildup: A case study of the magnetic storms in April 1997, *Geophys. Res. Lett., 25*, 3751, 1998.

Ejiri, M., Trajectory traces of charged particles in the magnetosphere, *J. Geophys. Res., 83*, 4798, 1978.

Elphic, R. C., L. A. Weiss, M. F. Thomsen, D. J. McComas, and M. B. Moldwin, Evolution of plasmaspheric ions at geosynchronous orbit during times of high geomagnetic activity, *Geophys. Res. Lett., 23*, 2189, 1996.

Fok, M.-C., Decay of ring current ions and associated aeronomical consequences, Ph.D. thesis, Univ. of Michigan, Ann Arbor, 1993.

Fok, M.-C., and T. E. Moore, Ring current modeling in a realistic magnetic field configuration, *Geophys. Res. Lett., 24*, 1775, 1997.

Fok, M-C., J. U. Kozyra, A. F. Nagy, C. E. Rasmussen, and G. V. Khazanov, A decay model of equatorial ring current and the associated aeronomical consequences, *J. Geophys. Res., 98*, 19,381, 1993.

Fok., M.-C., T. E. Moore, and M. E. Greenspan, Ring current development during storm main phase, *J. Geophys. Res., 101*, 15,311, 1996.

Fok, M.-C., R. A. Wolf, R. W. Spiro, and T. E. Moore, Comprehensive computational model of the Earth's ring current, *J. Geophys. Res.*, in press, 2001.

Friedrich, E., G. Rostoker, and M. G. Connors, Influence of the substorm current wedge on the *Dst* index, *J. Geophys. Res., 104*, 4567, 1999.

Garner, T. W., A case study of the June 4-5, 1991, magnetic storm using the Rice Convection Model, Ph.D. thesis, Rice Univ., Houston, Tex., 2000.

Gonzalez, W. D., J. A. Joselyn, Y. Kamide, H. W. Kroehl, G. Rostoker, B. T. Tsurutani, and V. M. Vasyliunas, What is a geomagnetic storm?, *J. Geophys. Res., 99*, 5771, 1994.

Gosling, J. T., The solar flare myth, *J. Geophys. Res., 98*, 18,937, 1993.

Grafe, A., Are our ideas about *Dst* correct?, *Ann. Geophys., 17*, 1, 1999.

Grande, M., C. H. Perry, J. B. Blake, M. Chen, J. Fennell, and J. L. Roeder, Evolution of the ring current ion population as observed by the CRRES/MICS instrument, *AIP Conf. Proc., 383*, 137, 1996.

Greenspan, M. E., and D. C. Hamilton, A test of the Dessler-Parker-Sckopke relation during magnetic storms, *J. Geophys. Res., 105*, 5419, 2000.

Gussenhoven, M. S., D. A. Hardy, and W. J. Burke, DMSP/F2 electron observations of equatorward auroral boundaries and their relationship to magnetospheric electric fields, *J. Geophys. Res., 86*, 768, 1981.

Gussenhoven, M. S., D. A. Hardy, and N. Heinemann, Systematics of the equatorward diffuse auroral boundary, *J. Geophys. Res., 88*, 5692, 1983.

Hamilton, D. C., G. Gloeckler, F. M. Ipavich, W. Studemann, B. Wilkey, and G. Kremser, Ring current development during the great geomagnetic storm of February 1986, *J. Geophys. Res., 93*, 14343, 1988.

Hedin, A. E., MSIS-86 thermospheric model, *J. Geophys. Res., 92*, 4649, 1987.

Huang, C. Y., and L. A. Frank, A statistical study of the central plasma sheet: Implications for substorm models, *Geophys. Res. Lett., 13*, 652, 1986.

Jordanova, V. K., J. U. Kozyra, G. V. Khazanov, A. F. Nagy, C. E. Rasmussen, and M.-C. Fok, A bounce-averaged kinetic model of the ring current ion population, *Geophys. Res. Lett., 21*, 2785, 1994.

Jordanova, V. K., L. M. Kistler, J. U. Kozyra, G. V. Khazanov, and A. F. Nagy, Collisional losses of ring current ions, *J. Geophys. Res., 101*, 111, 1996.

Jordanova, V. K., J. U. Kozyra, A. F. Nagy, and G. V. Khazanov, Kinetic model of the ring current-atmosphere interactions, *J. Geophys. Res., 102*, 14,279, 1997.

Jordanova, V. K., C. J. Farrugia, L. Janoo, J. M. Quinn, R. B. Torbert, K. W. Ogilvie, R. P. Lepping, J. T. Steinberg, D. J. McComas, and R. D. Belian, October 1995 magnetic cloud and accompanying storm activity: Ring current evolution, *J. Geophys. Res., 103*, 79, 1998a.

Jordanova, V.K., C. J. Farrugia, J. M. Quinn, R. M. Thorne, K. W. Ogilvie, R. P. Lepping, G. Lu, A. J. Lazarus, M. F. Thomsen, and R. D. Belian, Effects of wave-particle interactions on ring current evolution for January 10-11, 1997: Initial results, *Geophys. Res. Lett., 25*, 2971, 1998b.

Jordanova, V. K., R. B. Torbert, R. M. Thorne, H. L. Collin, J. L. Roeder, and J. C. Foster, Ring current activity during the early $Bz<0$ phase of the January 1997 magnetic cloud, *J. Geophys. Res., 104*, 24,895, 1999.

Kamide, Y., N. Yokoyama, W. Gonzalez, B. T. Tsurutani, I. A. Daglis, A. Brekke, and S. Masuda, Two-step development of geomagnetic storms, *J. Geophys. Res., 103*, 6917, 1998.

Korth, H., M. F. Thomsen, J. E. Borovsky, and D. J. McComas, Plasma

sheet access to geosynchronous orbit, *J. Geophys. Res., 104*, 25,047, 1999.

Kozyra, J. U., M.-C. Fok, E. R. Sanchez, D. S. Evans, D. C. Hamilton, and A. F. Nagy, The role of precipitation losses in producing the rapid early recovery phase of the great magnetic storm of February 1986, *J. Geophys. Res., 103*, 6801, 1998a.

Kozyra, J. U., V. K. Jordanova, J. E. Borovsky, M. F. Thomsen, D. J. Knipp, D. S. Evans, D. J. McComas, and T. E. Cayton, Effects of a high-density plasma sheet on ring current development during the November 2-6, 1993 magnetic storm, *J. Geophys. Res., 103*, 26,285, 1998b.

Kozyra, J. U., J. E. Borovsky, M. W. Chen, M.-C. Fok, and V. K. Jordanova, Plasma sheet preconditioning, enhanced convection, and ring current development, in *Substorms-4*, edited by S. Kokubun and Y. Kamide, Terra Sci., Tokyo, 1998c.

Lennartsson, W., and E. G. Shelley, Survey of 0.1- to 16-keV/e plasma sheet ion composition, *J. Geophys. Res., 91*, 3061, 1986.

Lepping, R. P., et al., The WIND magnetic field investigation, The Global Geospace Mission, *Space Sci. Rev., 71*, 207, 1995.

Liemohn, M. W., G. V. Khazanov, and J. U. Kozyra, Banded electron structure formation in the inner magnetosphere, *Geophys. Res. Lett., 25*, 877, 1998.

Liemohn, M. W., J. U. Kozyra, V. K. Jordanova, G. V. Khazanov, M. F. Thomsen, and T. E. Cayton, Analysis of early phase ring current recovery mechanisms during geomagnetic storms, *Geophys. Res. Lett., 25*, 2845, 1999.

Maynard, N. C., and A. J. Chen, Isolated cold plasma regions: Observations and their relation to possible production mechanisms, *J. Geophys. Res., 80*, 1009, 1975.

McComas, D. J., S. J. Bame, B. L. Barraclough, J. R. Donart, R. C. Elphic, J. T. Gosling, M. B. Moldwin, K. R. Moore, and M. F. Thomsen, Magnetospheric plasma analyzer: Initial three-spacecraft observations from geosynchronous orbit, *J. Geophys. Res., 98*, 13,453, 1993.

McComas, D. J., J. T. Gosling, and R. M. Skoug, Ulysses observations of the irregularly structured mid-latitude solar wind during the approach to solar maximum, *Geophys. Res. Lett., 27*, 2437, 2000.

McIlwain, C. E., A Kp dependent equatorial electric field model, *Adv. Space Res., 6*(3), 187, 1986.

McPherron, R. L., The role of substorms in the generation of magnetic storms, in *Magnetic Storms, Geophys. Monogr. Ser.*, vol. 98, edited by B. T. Tsurutani, et al., pp. 131-147, AGU, Washington, D. C., 1997.

Moldwin, M. B., M. F. Thomsen, S. J. Bame, D. J. McComas, and K. R. Moore, An examination of the structure and dynamics of the outer plasmasphere using multiple geosynchronous satellites, *J. Geophys. Res., 99*, 11,475, 1994.

Moore, T. E., et al., Ionospheric mass ejection in response to a CME, *Geophys. Res. Lett., 26*, 2339, 1999.

Ober, D. M., J. L. Horwitz, M. F. Thomsen, R. C. Elphic, D. J. McComas, R. D. Belian, and M. B. Moldwin, Premidnight plasmaspheric "plumes," *J. Geophys. Res., 102*, 11,325, 1997.

O'Brien, T. P., and R. L. McPherron, An empirical phase space analysis of ring current dynamics: Solar wind control of injection and decay, *J. Geophys. Res., 105*, 7707, 2000.

Ogilvie, K. W., et al., SWE, A comprehensive plasma instrument for the WIND spacecraft, The Global Geospace Mission, *Space Sci. Rev., 71*, 55, 1995.

Press, W. H., S. A. Teukolsky, W. T. Vetterling, and B. P. Flannery, *Numerical Recipes in FORTRAN*, 2nd ed., p. 352, Cambridge Univ. Press, New York, 1992.

Papitashvili, V. O., B. A. Belov, D. S. Faermark, Y. I. Feldstein, S. A. Golyshev, L. I. Gromova, and A. E. Levitin, Electric potential patterns in the northern and southern polar regions parameterized by the interplanetary magnetic field, *J. Geophys. Res., 99*, 13,251, 1994.

Rairden, R. L., L. A. Frank, and J. D. Craven, Geocoronal imaging with Dynamics Explorer, *J. Geophys. Res., 91*, 13,613, 1986.

Rasmussen, C. E., S. M. Guiter, and S. G. Thomas, Two-dimensional model of the plasmasphere: Refilling time constants, *Planet. Space Sci., 41*, 35, 1993.

Richmond, A. D., and Y. Kamide, Mapping electrodynamic features of the high-latitude ionosphere from localized observations: Technique, *J. Geophys. Res., 93*, 5741, 1988.

Roeder, J. L., J. F. Fennell, M. W. Chen, M. Grande, S. Livi, and M. Schulz, CRRES observations of stormtime ring current ion composition, in *Workshop on the Earth's Trapped Particle Environment*, edited by G. D. Reeves, *AIP Conf. Proc., 383*, 131, 1996.

Roelof, E. C., Energetic neutral atom image of storm-time ring current, *Geophys. Res. Lett., 14*, 652, 1987.

Sckopke, N., A general relation between the energy of trapped particles and the disturbance field near the Earth, *J. Geophys. Res., 71*, 3125, 1966.

Shue, J.-H., et al., Magnetopause location under extreme solar wind conditions, *J. Geophys. Res., 103*, 17,691, 1998.

Shue, J.-H., P. Song, C. T. Russell, J. K. Chao, and Y.-H. Yang, Toward predicting the position of the magnetopause within geosynchronous orbit, *J. Geophys. Res., 105*, 2641, 2000.

Siscoe, G. L., and N. U. Crooker, On the partial ring current contribution to *Dst*, *J. Geophys. Res., 79*, 1110-1112, 1974.

Sojka, J. J., C. E. Rasmussen, and R. W. Schunk, An interplanetary magnetic field dependent model of the ionospheric convection electric field, *J. Geophys. Res., 91*, 11,281, 1986.

Stern, D. P., The motion of a proton in the equatorial magnetosphere, *J. Geophys. Res., 80*, 595, 1975.

Sugiura, M., and T. Kamei, Equatorial *Dst* Index 1957-1986, ISGI Publ. Off., Saint-Maur-des-Fosses, France, 1991.

Takahashi, S., T. Iyemori, and M. Takeda, A simulation of the storm-time ring current, *Planet. Space Sci., 38*, 1133, 1990.

Thomsen, M. F., J. E. Borovsky, D. J. McComas, R. C. Elphic, and S. Maurice, The magnetospheric response to the CME passage of January 10-11, 1997, as seen at geosynchronous orbit, *Geophys. Res., Lett., 25*, 2545, 1998.

Tsurutani, B. T., and W. D. Gonzalez, The interplanetary causes of magnetic storms: A review, in *Magnetic storms, Geophys. Monogr. Ser.*, vol. 98, p. 77, edited by B. T. Tsurutani, et al., AGU, Washington, D. C., 1997.

Turner, N. E., D. N. Baker, T. I. Pulkkinen, and R. L. McPherron, Evaluation of the tail current contribution to *Dst*, *J. Geophys. Res., 105*, 5431, 2000.

Vassiliadis, D., A. J. Klimas, J. A. Valdivia, and D. N. Baker, The *Dst* geomagnetic response as a function of storm phase and amplitude and the solar wind electric field, *J. Geophys. Res., 104*, 24,957, 1999.

Volland, H., A semiempirical model of large-scale magnetospheric electric fields, *J. Geophys. Res., 78*, 171, 1973.

Watari, S., and T. Watanabe, The solar drivers of geomagnetic disturbances during solar minimum, *Geophys. Res. Lett., 25*, 2489, 1998.

Weimer, D. R., A flexible, IMF dependent model of high-latitude electric potentials having "space weather" applications, *Geophys. Res. Lett., 23*, 2549, 1996.

Weiss, L. A., R. L. Lambour, R. C. Elphic, and M. F. Thomsen, Study of plasmaspheric evolution using geosynchronous observations and global modeling, *Geophys. Res. Lett., 24*, 599, 1997.

Wilken, B., W. Weiss, D. Hall, M. Grande, F. Sørass, and J. F. Fennell, Magnetospheric ion composition spectrometer onboard the CRRES spacecraft, *J. Spacecr. Rockets, 29*, 585, 1992.

Yanenko, N. N., *The Method of Fractional Steps: The Solution of Problems of Mathematical Physics in Several Variables*, Springer-Verlag, New York, 1971.

Young, D. T., H. Balsiger, and J. Geiss, Correlations of magnetospheric ion composition with geomagnetic and solar activity, *J. Geophys. Res., 87*, 9077, 1982.

J. E. Borovsky, T. E. Cayton, and M. F. Thomsen, MS D-466, Los Alamos National Laboratory, Los Alamos, NM 87545. (jeborovksy@lanl.gov; tecayton@lanl.gov; mthomsen@lanl.gov)

J. U. Kozyra and M. W. Liemohn, Space Physics Research Laboratory, 2455 Hayward St., University of Michigan, Ann Arbor, MI 48109-2143. (jukozyra@umich.edu; liemohn@umich.edu)

G. Lu, High-Altitude Observatory, NCAR, Boulder, CO 80307-3000. (ganglu@hao.ucar.edu)

J. L. Roeder, Aerospace Corporation, Mail Stop: M2-260, P. O. Box 92957, Los Angeles, CA 90009-2957. (James.L.Roeder@aero.org)\

(Received August 25, 2000; revised November 6, 2000; accepted December 12, 2000.)